

Linear and nonlinear frequency-domain modelling of oscillatory flow over submerged canopies

Otto E. Neshamar, Niels G. Jacobsen, Dominic A. van der A & Tom O'Donoghue

To cite this article: Otto E. Neshamar, Niels G. Jacobsen, Dominic A. van der A & Tom O'Donoghue (2023) Linear and nonlinear frequency-domain modelling of oscillatory flow over submerged canopies, Journal of Hydraulic Research, 61:5, 668-685, DOI: [10.1080/00221686.2023.2231433](https://doi.org/10.1080/00221686.2023.2231433)

To link to this article: <https://doi.org/10.1080/00221686.2023.2231433>



© 2023 The Author(s). Published by Informa UK Limited, trading as Taylor & Francis Group.



Published online: 15 Sep 2023.



Submit your article to this journal [↗](#)



View related articles [↗](#)





View Crossmark data [↗](#)





Research paper

Linear and nonlinear frequency-domain modelling of oscillatory flow over submerged canopies

OTTO E. NESHAMAR , PhD Student, *School of Engineering, University of Aberdeen, AB24 3UE Aberdeen, UK*
Email: o.neshamar@abdn.ac.uk (author for correspondence)

NIELS G. JACOBSEN , Lead Engineer Hydrodynamics, *Vattenfall Vindkraft A/S, Ørestads Blvd. 108, 2300 Copenhagen, Denmark*
Email: nielsgoel.jacobsen@vattenfall.com

DOMINIC A. VAN DER A , Lecturer, *School of Engineering, University of Aberdeen, AB24 3UE Aberdeen, UK*
Email: d.a.vandera@abdn.ac.uk

TOM O'DONOGHUE , Professor, *School of Engineering, University of Aberdeen, AB24 3UE Aberdeen, UK*
Email: t.odonoghue@abdn.ac.uk

ABSTRACT

An analytical and experimental study of flow velocities within submerged canopies of rigid cylinders under oscillatory flows is presented, providing insights into the momentum transfer mechanisms between the different flow harmonics. The experimental dataset covers an unprecedented wide range of flow amplitudes with in-canopy velocity reductions ranging between 0.2 and 0.8 of the free stream velocity (from inertia- to drag-dominated in-canopy flow). Results from the analytical model with nonlinear drag compare favourably to the experimental data. Having application of theories for free surface waves over canopies in mind, the effects of linearization of the drag are analysed by comparing sinusoidal and nonlinear model predictions. Finally, a unified prediction formula for in-canopy velocities for sinusoidal, velocity-skewed, and velocity-asymmetric free stream velocities is presented. The formula depends on two non-dimensional parameters related to inertia and drag forces, and the unified formula allows for easy assessment of the maximum in-canopy velocity.

Keywords: Canopies; drag force; nonlinear momentum transfer; oscillatory flow; velocity reduction

1 Introduction

The implementation of nature-based (green) coastal protection has received considerable attention in recent years. Recent reviews of the topic include Jordan and Fröhle (2022), Schoonees et al. (2019) and Morris et al. (2018), and several practical guidelines for implementing nature-based solutions in flood risk management have been developed (Bridges et al., 2022; CISL, 2022; The European Commission, 2021; The World Bank, 2017). However, nature-based solutions are still characterised by significant uncertainties in their cost and potential impact, leading to a continued demand for research in order to quantify and limit these uncertainties.

In relation to coastal engineering, the vast majority of research has focused on wave attenuation by submerged and emergent vegetation canopies, based on either analytical and

numerical modelling (e.g. Cao et al., 2015; Méndez et al., 1999; Van Rooijen et al., 2020) or on direct measurements in the field or in laboratories (e.g. Anderson & Smith, 2014; He et al., 2019; Jadhav et al., 2013; Möller et al., 2014). Much of the experimental work has involved canopies of flexible vegetation (Mullarney & Henderson, 2018). In the present paper, the vegetation is represented as a canopy of rigid cylinders in order to address fundamental aspects of the hydrodynamic processes.

For waves propagating over a vegetated bed, the in-canopy velocities are important for wave attenuation and sediment dynamics (Jacobsen et al., 2019; Jadhav et al., 2013). Velocities within the canopy are lower than the wave-generated free-stream velocity above the canopy. Research thus far has established that the smallest velocity reduction occurs in the inertia-dominated regime corresponding to $a_1/S \lesssim 1$, where a_1 is the free-stream orbital amplitude and S is the average spacing

Received 9 May 2022; accepted 21 June 2023/Currently open for discussion.

between stems (Lowe et al., 2005; Pujol et al., 2013; Van Rooijen et al., 2020), while higher velocity reduction occurs when $a_1/S > 1$, as the flow-canopy interaction becomes increasingly drag dominated. This work extends the existing empirical evidence with experiments involving high free-stream velocities reaching well into the drag-dominated regime, and investigates a closed form prediction formulation for the in-canopy velocity reduction based on non-dimensional quantities.

Four approaches can be identified for determining in-canopy velocities under wave-driven oscillatory flow, each approach having its specific application and merits: (i) oscillatory time-domain solutions with nonlinear drag and numerical integration of the momentum equation (Lowe et al., 2005; Zeller et al., 2015); (ii) analytical solutions for free surface wave propagation in submerged and emergent vegetation (Asano et al., 1992; Dubi & Tørum, 1994; Jacobsen, 2016; Kobayashi et al., 1993; Méndez et al., 1999), for which a linearization of the drag term is used through the Lorentz’ principal of identical work (e.g. Sollitt & Cross, 1972); (iii) simulation of the flow field using complex depth-resolving models (Chen & Zou, 2019; Van Rooijen et al., 2020); and (iv) laboratory or field measurements (Lowe et al., 2005; Pujol et al., 2013; Van Rooijen et al., 2020). With respect to approach (ii), it is important to note that the validity of linearizing the drag has not been properly addressed in the literature, even though the linearization leads to analytical expressions for radiation stress tensors (Jacobsen, 2016; Mendez et al., 1998), Lagrangian Stokes drift (Jacobsen, 2016; Jacobsen & McFall, 2022), and vertical distributions of shear stress (Jacobsen & McFall, 2022), all of which can be readily implemented in large-scale hydrodynamic models using the procedure outlined in Jacobsen and McFall (2022) for coupling between spectral wave models and large-scale hydrodynamic models based on the shallow water equations. Models for the mean wave-induced current in canopies have been proposed by Luhar et al. (2010) and Van Rooijen et al. (2020), for which the in-canopy velocity reduction is of implicit importance.

The present work examines the oscillatory flow velocity within a rigid canopy, with particular focus on the formulation for the drag force in the governing equations. This is achieved through a combination of analytical modelling and laboratory experiments in a large-scale oscillatory flow tunnel. Two frequency-domain models, one with nonlinear drag and one with a sinusoidal velocity response akin to Airy wave theory in which the drag is linearized, are described in Section 2 and the experiments are presented in Section 3. The analytical models are validated against the experimental data in Section 4.1 and subsequently the models are compared for a wider range of hydrodynamic and canopy conditions than covered by the experiments. A practical engineering prediction model for in-canopy velocity reduction is proposed in Section 4.4. Section 5 discusses implications of the results for modelling nonlinear surface waves in the presence of canopies and for sediment transport. The conclusions are presented in Section 6.

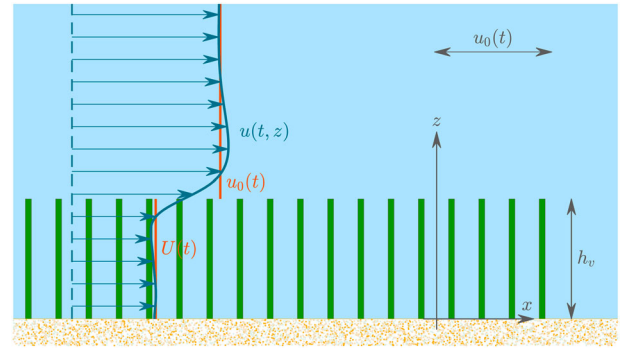


Figure 1 Definition sketch for oscillating (tunnel) spatially averaged flow with submerged, rigid vegetation. The analytical domain is vertically unbounded. u_0 is the bulk free stream velocity, $U(t)$ is the bulk in-canopy velocity and the blue $u(t, z)$ is the velocity profile including viscous effects

2 Mathematical model

2.1 Governing equations

In the present work, pure oscillatory (tunnel) spatially-averaged flow is considered, which means there is no organized, vertical velocity ($w = 0 \text{ m s}^{-1}$). It is furthermore assumed in the analytical derivation that the flow is unbounded along the positive and vertical z -axis and that the canopy stems are rigid. The theoretical domain is depicted in Fig. 1, where the spatially-averaged velocity profile (blue line) and the associated 2-layer solution to the bulk velocities (red lines) are shown. The authors arrive at governing equations of the same form as Lowe et al. (2005), Luhar et al. (2010), Zeller et al. (2015) (with minor differences in the canopy shear term). The present work applies these equations in the frequency domain to investigate the required number of harmonics for an accurate solution and to validate against experiments with large free stream velocity amplitudes.

The pure oscillatory and spatially averaged flow along the x -axis means that $\partial/\partial x = \partial/\partial y = 0$ when applied to any quantity. The continuity equation thus reads:

$$\frac{\partial u}{\partial x} + \frac{\partial v}{\partial y} + \frac{\partial w}{\partial z} = \frac{\partial w}{\partial z} = 0 \quad (1)$$

which means $w = 0$ for all z in order to satisfy the no-slip condition at the bottom. Inserting $w = 0$ in the vertical momentum equation for the flow in porous media (e.g. Jensen et al., 2014), it follows that $\partial p/\partial z = 0$, i.e. the pressure is hydrostatic over the vertical. Finally, the horizontal momentum equation takes the following form (see Appendix A.1):

$$\left(1 + C_m N \frac{d^2}{4} \pi\right) \frac{\partial u}{\partial t} = -\frac{1}{\rho} \frac{\partial p}{\partial x} + \frac{1}{n} \frac{\partial}{\partial z} (v + v_t) \frac{\partial u}{\partial z} - F_D \quad (2)$$

Here, in the momentum equation for porous flow the filter velocity u is used (Jensen et al., 2014). C_m is the added mass coefficient for the individual stem with circular cross-section and diameter d , N is the number of stems per unit area, n is the

porosity ($n = 1 - \lambda$, with $\lambda = Nd^2\pi/4$ being solidity, as used by other authors), ρ is fluid density, ν and ν_t are the molecular and eddy viscosities, and F_D is the fluid drag. Above the canopy $\lambda = N = F_D = 0$ and $n = 1$. In the following, we use Γ_I for $(1 + C_m Nd^2\pi/4)/n$. The filter velocity is the average velocity over the entire cross section (water and stems), while the pore velocity is the average velocity over the water part of the cross section. The relationship reads $u = nu_p$, where subscript p denotes the pore velocity.

Far above the canopy (away from the canopy shear layer) Eq. (2) reduces to:

$$\frac{\partial u}{\partial t} = \frac{\partial u_0}{\partial t} = -\frac{1}{\rho} \frac{\partial p}{\partial x} \quad (3)$$

where u_0 is the free stream velocity. Since $\partial p/\partial z = 0$, substitution of $-\frac{1}{\rho} \partial p/\partial x$ with the prescribed free stream acceleration ($\partial u_0/\partial t$) is also valid within the canopy. The drag on the stems is defined as:

$$F_D = \frac{1}{2} C_D P(n) N d |u| u \quad (4)$$

where $P(n)$ is a function that accounts for whether filter or pore velocities are applied for the evaluation of the drag (see discussion in Etminan et al., 2019). In the present work, the drag force in the model is based on pore velocity, because the measured drag coefficients are based on measured pore velocities (see Section 3), so $P(n) = n^{-2}$. C_D is the drag coefficient.

Our focus is not on predicting the vertical profile of horizontal velocity, but rather on the overall performance of linear versus nonlinear drag formulations in predicting the bulk in-canopy velocity. For this reason, a two-layer solution is adopted, akin to the work by Lowe et al. (2005), where the diffusion term in Eq. (2) is replaced by a shear stress at the top of the canopy (the shear at the bottom is proportional to the drag and is absorbed into C_D , see Appendix A.2):

$$\Gamma_I \frac{\partial U}{\partial t} = \frac{\partial u_0}{\partial t} + \frac{C_f}{h_v} |\Delta U| \Delta U - \frac{1}{2} C_D P N d |U| U \quad (5)$$

where U is the bulk in-canopy filter velocity, $\Delta U = u_0 - U$ is the velocity difference between the in-canopy and free stream velocities, and C_f is a friction factor for the shear layer on top of the canopy. U is defined as the vertical average over the canopy height h_v (Appendix A.2). Note that following Eq. (3), the ‘‘bulk’’ velocity above the canopy equals u_0 . Lowe et al. (2005) described the canopy shear based on the free stream velocity, while the present model describes the shear contribution in terms of the velocity deficit in order to account for the influence of the in-canopy velocity U on canopy shear, as outlined by Zeller et al. (2015). For very short and sparse canopies, the bottom friction may have important contributions to the momentum balance; however, bottom friction is still parameterized as proportional to $|U|U$ without accounting for phase leads between in-canopy velocity and bottom shear stress, so an

appropriate correction to C_D covers this scenario in the present two-layer model. The bottom boundary layer must be resolved to accurately account for phase lead effects between in-canopy velocity and bottom shear stress, which is often impossible for large-scale hydrodynamic models based on the shallow-water equations.

The following non-dimensional parameters (indicated with a circumflex accent) are introduced: $\hat{U} = U/u_1$, $\hat{u}_0 = u_0/u_1$, $\hat{t} = t\omega$. The characteristic dimensional quantities are the amplitude of the first harmonic of the free stream velocity, u_1 , and the cyclic frequency $\omega = 2\pi/T$, where T is the oscillatory flow period.¹ This gives the following non-dimensional form of the momentum equation for \hat{U} :

$$\Gamma_I \frac{\partial \hat{U}}{\partial \hat{t}} = \frac{\partial \hat{u}_0}{\partial \hat{t}} + \Gamma_f |\Delta \hat{U}| \Delta \hat{U} - \Gamma_D |\hat{U}| \hat{U} \quad (6)$$

which shows that the in-canopy velocity is governed by three non-dimensional parameters:

$$\Gamma_I = \frac{1}{n} \left(1 + C_m \frac{d^2}{4} \pi N \right), \quad \Gamma_f = \frac{C_f a_1}{h_v}, \quad \Gamma_D = \frac{C_D}{2} P N d a_1 \quad (7)$$

related to inertia (Γ_I), canopy interface friction (Γ_f), and drag on the stems (Γ_D). $a_1 = u_1/\omega$ is the free stream orbital amplitude of the first harmonic. It is seen that the importance of the friction is inversely proportional to the height of the canopy. The parameter $N d a_1 \propto (d/S) \cdot (a_1/S)$ is the product of the two governing parameters proposed by Lowe et al. (2005), where $S \propto N^{-1/2}$ is the spacing between the stems. In the following derivations, the $\hat{\cdot}$ is omitted; however, it is reintroduced in Section 4 to distinguish between dimensional and non-dimensional quantities.

Non-dimensional solutions to the free stream and in-canopy velocities of the following forms are considered:

$$u_0 = \frac{1}{2} \sum_{m=1}^M [u_m e^{imt} + c.c.], \quad U = \frac{1}{2} \sum_{m=1}^M [U_m e^{imt} + c.c.] \quad (8)$$

where $c.c.$ is the complex conjugate and M is the number of harmonics. The formulation for U explicitly allows for phase lags between the harmonics U_m .

2.2 Sinusoidal solution

Free surface wave models over submerged and emerging canopies based on linear wave theory are often derived with a linearized drag term, which results in sinusoidal flow velocities throughout the water column (Asano et al., 1992; Jacobsen, 2016; Méndez et al., 1999). Analogous to these linearized free surface models, a model for the in-canopy velocity is derived here for $M = 1$, and it is termed the ‘‘sinusoidal model’’

throughout. We assume that the friction and drag can be linearized in the following fashion:

$$\Gamma_f |\Delta U| \Delta U + \Gamma_D |U| U = \Gamma_{L,f} \Delta U + \Gamma_{L,D} U \quad (9)$$

Here, $\Gamma_{L,f}$ and $\Gamma_{L,D}$ are the linearized friction and drag parameters. The equality is fulfilled by equalizing the energy dissipation over one wave period (Sollitt & Cross, 1972) separately for friction and drag:

$$\Gamma_{L,f} \overline{\Delta U^2} = \Gamma_f \overline{|\Delta U| \Delta U^2} \quad \text{and} \quad \Gamma_{L,D} \overline{U^2} = \Gamma_D \overline{|U| U^2} \quad (10)$$

where the overline means period-averaging. This linearization based on identical energy dissipation is adopted from free surface wave models, where it corresponds to matching of the wave attenuation across a canopy, and it is employed here in order to ensure that the model can be used in conjunction with the aforementioned free surface models. The parameters $\Gamma_{L,f}$ and $\Gamma_{L,D}$ are found numerically. Inserting Eqs (8) and (9) in Eq. (6), it follows that:

$$\Gamma_I i U_1 = (i + \Gamma_{L,f}) u_1 - (\Gamma_{L,f} + \Gamma_{L,D}) U_1 \quad (11)$$

Here, subscript “1” means that only the first harmonic (sinusoidal) component is included. Therefore:

$$U_1 = \frac{(i + \Gamma_{L,f})}{i \Gamma_I + \Gamma_{L,f} + \Gamma_{L,D}} u_1 = G_L u_1 \quad (12)$$

The final expression shows that the in-canopy velocity is in-phase with the free stream velocity for inertia dominated flows (imaginary part of G_L goes to 0), while increasing influence of drag and friction gives rise to a phase lead of the in-canopy flow over the free stream velocity (maximum phase lead is $\pi/2$, when the real part of G_L goes to zero).

2.3 Nonlinear solution

To obtain a nonlinear solution, the following Fourier expansions are introduced:

$$|\Delta U| = b_0 + \frac{1}{2} \sum_{q=1}^{\infty} [b_q e^{iqt} + c.c] \quad (13a)$$

$$|U| = B_0 + \frac{1}{2} \sum_{q=1}^{\infty} [B_q e^{iqt} + c.c] \quad (13b)$$

The products $|\Delta U| \Delta U = |u_0 - U|(u_0 - U)$ and $|U| U$ can be given in Fourier terms by evaluating the products of the expansions in Eqs (8), (13a) and (13b). These products suggest that there will be an exchange of momentum between the frequencies; the momentum exchange is mathematically identical to the generation of super- and subharmonics in free surface wave theory (Madsen & Fuhrman, 2006). Inserting Eqs (8), (13a) and

(13b) into Eq. (6), the following momentum equation for the m th harmonic is found:

$$\Gamma_I i m U_m = i m u_m + \Gamma_f \left[b_0 \Delta U_m + b_q \Delta U_l + G(b_p^* \Delta U_k) \right] - \Gamma_D \left[B_0 U_m + B_q U_l + G(B_p^* U_k) \right] \quad (14)$$

where * means the complex conjugate and $\Delta U_m = u_m - U_m$. The indices are such that $m = q + l$ (super-harmonic interaction for all $q > 0$ and $l > 0$) and $m = |k - p|$ (sub-harmonic interaction for all $k > 0$ and $p > 0$). The function G reads:

$$G(\varphi_{pk}) = \begin{cases} \varphi_{pk} & \text{for } k - p > 0 \\ \varphi_{pk}^* & \text{for } k - p < 0 \end{cases} \quad (15)$$

Introducing the decomposition $U_m = U_{r,m} + i U_{i,m}$, where superscripts r and i refer to the real and imaginary components, and treating $U_{r,m}$ and $U_{i,m}$ as separate variables, Eq. (14) can be written as a $2M \times 2M$ matrix system with a non-homogeneous right-hand side. The matrix system is nonlinear, because the coefficients b_q and B_q for $q = 0, 1, 2, \dots$ depend on all components in U . The matrix system is solved by successively inserting the solution from previous iterations until converged below a 2-norm of 10^{-10} . $M = 21$ is used throughout the present analysis, and Eqs (13a) and (13b) are evaluated with $2M$ components to incorporate all sub-harmonic contributions.

The momentum equation (Eq. (6)) is, as already discussed, practically identical to the two-layer models proposed by Lowe et al. (2005) and Zeller et al. (2015). However, the main difference is the solution procedure: where their models were solved in the time-domain, the present sinusoidal and nonlinear models are solved in the frequency domain, which has the advantage that the in-canopy momentum distribution (e.g. $|U_2|/|U_1|$, $|U_3|/|U_1|, \dots$) is obtained directly without additional post-processing and the super- and sub-harmonic interactions are quantified. This advantage will be utilized in Section 4.3, where momentum distribution, momentum exchange, and importance of super- and sub-harmonic terms are quantified for sinusoidal and velocity-skewed free stream velocities.

3 Experiments

3.1 Experimental set-up

The experiments were performed in the Aberdeen Oscillatory Flow Tunnel (AOFT) (Fig. 2). The test section is 10 m long, 0.3 m wide and 0.75 m tall. A 7 m long false bed was installed at an elevation of 0.25 m above the tunnel floor within the test section with ramps of slope 1:4 at either end, reducing the effective flow depth within the test section to 0.5 m. Stiff, circular PVC rods, with $h_v = 130$ mm and $d = 8.3$ mm, were fixed to the false bed in a regular geometric pattern over its full

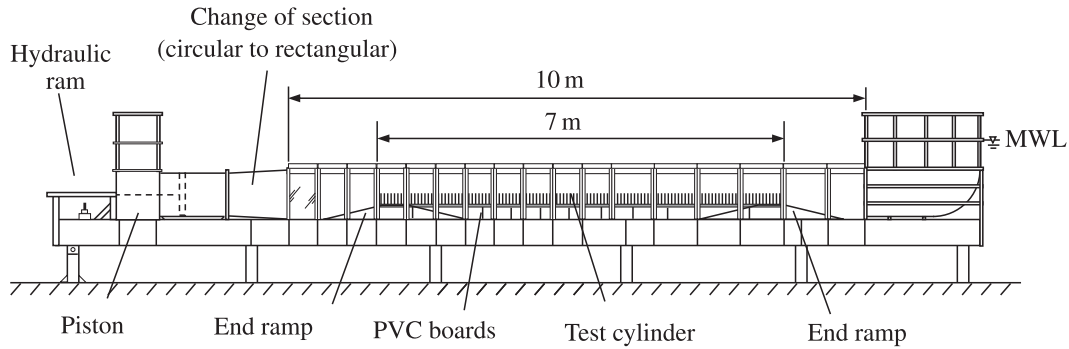


Figure 2 Layout of the AOFT with the rigid cylinder array installed on the false bottom. The force is measured on the test cylinder as described in Neshamar (2022)

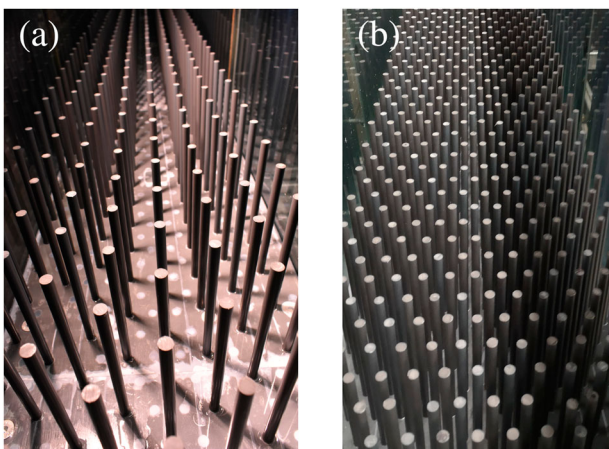


Figure 3 Pictures of (a) the sparse canopy and (b) the dense canopy

length. Two canopy densities were tested: a sparse canopy with $N = 579$ stems m^{-2} , shown in Fig. 3a, and a dense canopy with $N = 1736$ stems m^{-2} , shown in Fig. 3b. The corresponding porosities are $n = 0.969$ and $n = 0.906$, respectively. These array densities were selected to resemble submerged vegetation canopies, for which porosities of 0.9–0.99 were reported by Nepf (2012). One rod in the centre of the canopy (~ 3.5 m from the leading edge of the canopy) was mounted on a force transducer (ATI Nano17 IP68 6-axis load cell) built into the false bed to measure forces from which the hydrodynamic force coefficients could be determined. The load cell measures forces and moments along all three axes and can be operated in three different calibration settings, with sensing ranges of 12–50 N for force and 120–500 N mm for moment; the corresponding measurement resolutions are 0.003–0.013 N and 0.016–0.063 N mm.

For each canopy density, experiments were conducted for five free stream velocity amplitudes with constant oscillatory flow period $T = 6$ s. The piston input signal was sinusoidal but the measured free-stream velocities showed slight departure from sinusoidal with higher harmonics present in the flow. The velocities were measured using a Dantec FibreFlow 2-component laser Doppler anemometer (LDA), consisting of

a 300 mW Ar-ion laser and F60 burst spectrum analyser, operating in back-scatter mode. During the LDA experiments, the water was seeded with Spherical 110P8 hollow glass microspheres of 9–13 μm diameter. Accurate positioning of the measurement volume was achieved with the LDA probe mounted on a 3-axis computer-controlled traverse that enables x , y and z positioning with a resolution of 12.5 μm . Measurements were made over 100 flow periods, with data rates typically higher than 100 Hz (depending on seeding and flow velocity). The measured data were processed to give 50 Hz phase-averaged velocity time-series.

The experimental conditions are listed in Table 1, including the magnitude and phase of the first three harmonics of the measured free-stream velocity. The free-stream orbital amplitudes had a range of 0.16–0.92 m, similar to near-bed orbital amplitudes under full-scale storm waves. With a total canopy length of 7 m, flow near the middle of the canopy is assumed to be minimally influenced by transitional features originating at the ends of the canopy, effectively resembling oscillatory flow through an infinitely long, uniform canopy. This assumption was validated with velocity measurements over a 30-cm range of x -locations and a range of y -locations (106 mm for the sparse array and 54 mm for the dense array) near the middle of the canopy, which showed no significant difference in phase-averaged flow velocities with x or y (see Neshamar, 2022, for a detailed description of these measurements). Flow in the middle of the tunnel is therefore minimally influenced by the finite length of the test section and the tunnel side walls.

The main velocity measurements were made near a cylinder in the middle of the array, adjacent to the instrumented cylinder. With the coordinate system centred at the base of the nearby cylinder, vertical profiles of flow velocities were measured at $x = -12$ mm (halfway between cylinder rows), for four y -positions in the case of the sparse canopy ($y = 0, 5.4, 12, 18.7$ mm) and three y -positions in the case of the dense canopy ($y = 0, 2.7, 5.3$ mm). For each vertical profile, velocities were measured at 11 vertical (z) positions over the canopy depth ($N_w = 11$, Table 1), and between 5 and 17 vertical positions above the canopy (N_a in Table 1).

Table 1 Overview of the ten experimental cases

Case	N [m ⁻²]	$ u_1 $ [m s ⁻¹]	$\arg u_1$ [°]	$ u_2 / u_1 $ [%]	$\arg u_2$ [°]	$ u_3 / u_1 $ [%]	$\arg u_3$ [°]	N_w [-]	N_a [-]	Γ_I [-]	Γ_D [-]	Γ_f [-]	δ_S [%]	δ_{NL} [%]	δ_{LKM} [%]
S1	579	0.17	-89	1.7	-89	5.0	-94	11	5	1.043	0.495	0.024	10.4	6.9	6.0
S2	579	0.37	-90	1.7	-50	3.4	-92	11	10	1.043	1.093	0.054	11.8	7.7	7.7
S3	579	0.51	-90	1.3	-66	2.9	-88	11	11	1.043	1.518	0.150	12.4	7.9	9.1
S4	579	0.73	-90	1.1	-62	2.4	-86	11	12	1.043	2.175	0.214	11.6	7.1	9.1
S5	579	0.95	-90	1.1	-41	2.0	-97	11	13	1.043	2.839	0.350	10.2	5.4	9.3
D1	1736	0.17	-90	1.8	-88	5.1	-101	11	10	1.137	2.630	0.034	16.1	6.3	9.9
D2	1736	0.37	-90	1.4	-97	4.0	-106	11	13	1.137	5.797	0.074	13.7	4.4	9.0
D3	1736	0.51	-90	1.4	-56	3.6	-98	11	14	1.137	8.047	0.093	13.9	3.8	8.7
D4	1736	0.73	-89	1.2	-70	3.1	-99	11	14	1.137	11.496	0.147	13.5	5.0	10.8
D5	1736	0.96	-90	0.9	-51	3.5	-71	11	17	1.137	15.186	0.127	14.5	6.2	11.0

Note: Cases S1–S5 have a sparse canopy and cases D1–D5 have a dense canopy. Case names are applied in Figs 8 and 10. u_1 , u_2 , and u_3 are free stream velocity amplitudes. N_w and N_a are the number of averaging points within and above the canopy, respectively. Γ_I , Γ_D , and Γ_f are non-dimensional resistance quantities. The normalized deviations to the experiments for the sinusoidal (δ_S), nonlinear (δ_{NL}), and Lowe et al. (2005) (δ_{LKM}) models are defined in Section 4.1.

3.2 Local and spatial averaged velocities

Figure 4 shows the x – y positions of the in-canopy measurement positions; the positions form a row of approximately evenly-spaced points spanning the periodic domain along y . The effective number of velocity profiles is doubled because of a “mirroring” effect: since the array geometry is symmetric, and the free-stream velocity is approximately sinusoidal, phase-averaged velocities around each cylinder will be opposite in magnitude along x but otherwise identical during the first and second halves of the flow cycle. Consequently, measurements of the “local velocity” u_l at a given “real” measurement

coordinate can represent an additional measurement at the “mirror” position by inverting the measured velocity time-series and phase-shifting by 180°. For example, u_l recorded at a position immediately in front of a cylinder in the first flow half-cycle is equal to $-u_l$ recorded at a point immediately behind the cylinder in the second half-cycle.

Since phase-averaged vertical velocities within the array are negligible, in-canopy flow is effectively divided into thin horizontal “layers” with negligible mass transfer between layers. From continuity, the spatially-averaged filter velocity, $u_e(z, t)$ (subscript e refers to experimental value), is therefore found by averaging velocities along y at $x = -S_x/2$, where S_x is the cylinder centre-to-centre spacing along x . The spatially-averaged filter velocity was obtained by interpolating the velocity measurements (real and mirrored) onto an evenly-spaced grid spanning the periodic domain along y , and averaging the result. This procedure results in an approximation of u_e , which assumes the overall flow to be fully periodic and symmetric. Due to the mirroring, the calculated u_e is symmetric in time and contains no even-numbered harmonics. Neshamar (2022) describes how this method was validated experimentally, by comparison with measurements made along two different y -transects (at $x = -S_x/2$ and $x = -S_x/4$).

The depth- and spatially-averaged in-canopy filter velocity, U_e , is found through vertical integration:

$$U_e(t) = \frac{1}{h_v} \int_0^{h_v} u_e dz \tag{16}$$

whereby the bulk pore velocity follows: $U_{e,p} = U_e/n$.

3.3 Force coefficients

Hydrodynamic force on a cylinder is determined from the Morison equation, where the spatially-averaged pore velocity

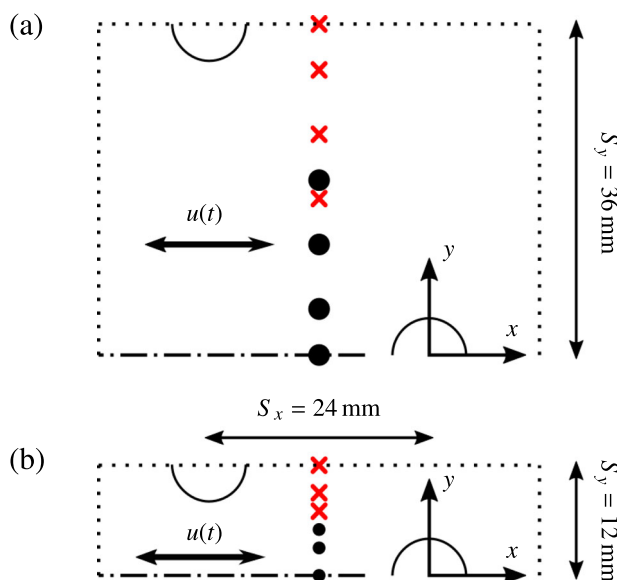


Figure 4 Periodic representation of the (a) sparse and (b) dense array geometries viewed from above. The dashed line at the bottom of each figure indicates symmetry, and the dotted lines around the other three sides indicate periodic boundaries. The figures show the coordinates where vertical profiles were measured (●), as well as corresponding “mirrored” coordinates based on symmetry of geometry and flow characteristics (X) as described in Section 3.2

$(u_{e,p} = u_e/n)$ is used as the characteristic velocity:

$$F_x(z) = \frac{1}{2} \rho C_D d |u_{e,p}| u_{e,p} + \rho(1 + C_m) \frac{d^2 \pi}{4} \frac{\partial u_{e,p}}{\partial t} \quad (17)$$

where $F_x(z)$ is the in-line force per unit length at elevation z . Note that force varies with z due to variations in $u_{e,p}$ (Fig. 10); the coefficients C_D and C_m are assumed constant with z . The added mass coefficient C_m can, in principle, be estimated directly from force measurements. However, since the associated force is much smaller than the drag force under the present conditions, there is large uncertainty when estimating C_m from the measurements. Instead, the established value of $C_m \approx 1$ is used in the present work (e.g. Sumer & Fredsøe, 1999).

Since the load cell measures moments with a higher resolution compared to the forces, the drag coefficient C_D is calculated from the moment measurements. A force in the x -direction produces a moment about the y -axis, and the total moment applied to the load cell M_y can be calculated by multiplying the inline force (Eq. (17)) by the “lever-arm” and integrating vertically, i.e.:

$$M_y = M_{y,D} + M_{y,m} \quad (18a)$$

$$M_{y,D} = \frac{1}{2} \rho C_D d \int_0^{h_v} |u_{e,p}| u_{e,p} (z + z_{offset}) dz \quad (18b)$$

$$M_{y,m} = \rho(1 + C_m) \frac{d^4 \pi}{4} \int_0^{h_v} \frac{\partial u_{e,p}}{\partial t} (z + z_{offset}) dz \quad (18c)$$

where $M_{y,D}$ and $M_{y,m}$ are the components of moment due to drag and added mass, respectively, and $z_{offset} = 10$ mm is the vertical distance between the front face of the load cell and the tunnel floor. To determine C_D , $M_{y,m}$ is first calculated from Eq. (18c), with $C_m = 1$, obtaining the flow acceleration at each z using a central difference method, and performing the numerical integration along z by interpolating linearly between measurement points. The result is subtracted from the total moment measured by the load cell, $M_{y,LC}$, to produce a “measured” drag-related moment $M_{y,D,LC} = M_{y,LC} - M_{y,m}$. Using an initial value of $C_D = 1$, the actual value of C_D is then determined by matching the “predicted” $M_{y,D}$ time-series (Eq. (18b)) to the “measured” $M_{y,D,LC}$ time-series using a least-squares method (see e.g. Sumer & Fredsøe, 1999).

Figure 5 shows an example comparison between M_y measured by the load cell and the calculated M_y obtained using the method described above, which for this case (S4) results in a fitted drag coefficient of $C_D = 1.37$. The figure shows that the two curves match very well in both phase and shape, indicating that the given values of C_m and C_D are accurate. The same method was used to calculate C_D for all flow cases, and each case produced a similarly close match between measured and calculated moments as shown for the example case in Fig. 5.

Figure 6 shows the C_D values obtained from the moment measurements for all flow cases, presented as a function of Reynolds number, defined as $Re = U_{p,max} d / \nu$, where $U_{p,max}$ is

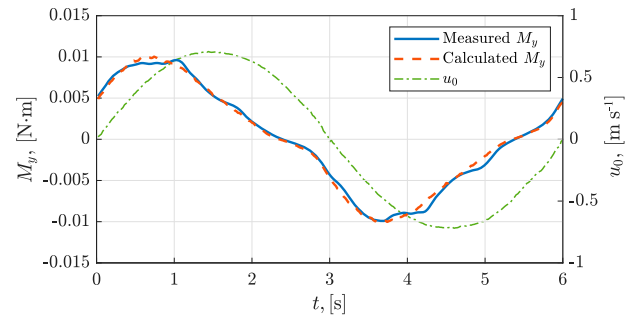


Figure 5 Measured and calculated moment around the y -axis M_y , case S4. The free-stream velocity u_0 is also shown for reference

the maximum in-canopy pore velocity. The figure also shows C_D from tests involving oscillatory flow past a single, isolated cylinder, which were conducted prior to the present series of experiments using the same experimental arrangement. Note that, for the isolated cylinder, the increase in C_D observed around $Re = 10^3$ is due to the onset of flow-induced vibrations, similar to those discussed by Neshamar et al. (2022). No vibrations were observed during canopy experiments. C_D in oscillatory flow is governed by Re and the Keulegan–Carpenter number $K_C = U_{p,max} T / d$. The experiments were conducted at a constant value of $Re/K_C = 11.5$, which means that the K_C values corresponding to the results in Fig. 6 are obtained from $K_C = Re/11.5$. C_D for a cylinder within an array is also influenced by array geometry: Etminan et al. (2019) hypothesized that C_D for a cylinder within an array is governed by two effects, namely “blockage” and ‘sheltering’. The blockage effect describes the locally increased flow velocity in the constricted space around the cylinder, which results in increased drag on the cylinder. Conversely, sheltering occurs when a cylinder is “hidden” in the wake of an upstream cylinder, and drag is reduced due to a lower incident velocity. Of the two mechanisms, their simulations showed the blockage effect to be dominant, particularly for high canopy densities. To account for the blockage effect, they proposed that C_D for a cylinder in an array can be quantified using the constricted velocity, u_c , defined as the velocity averaged over the constricted cross-sections around the cylinder. For the array layout shown in Fig. 4, u_c is related to u_p

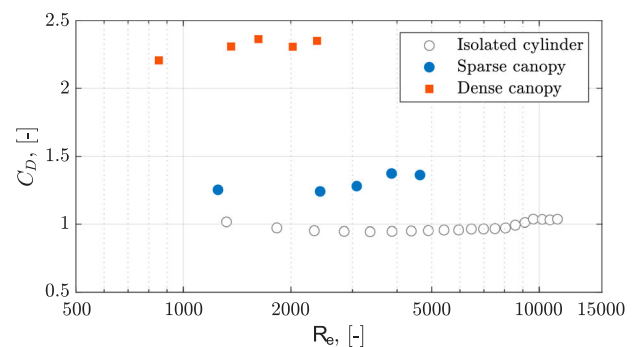


Figure 6 Drag coefficients obtained from moment measurements as a function of Reynolds number

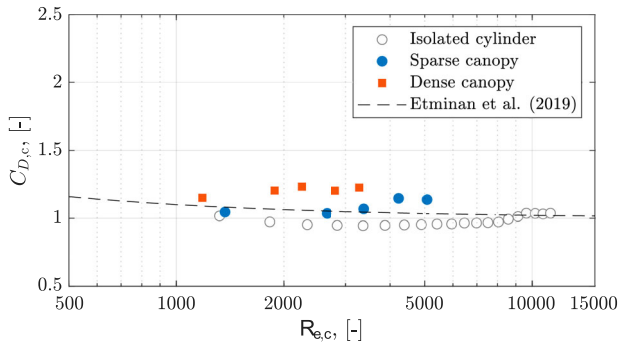


Figure 7 $C_{D,c}$ obtained from moment measurements as a function of constricted Reynolds number, with predicted values from Eq. (20) shown for comparison

by:

$$u_c = \frac{n}{1 - d/2S_y} u_p \quad (19)$$

where S_y is the cylinder centre-to-centre spacing along y . Based on this, a constricted Reynolds number, $R_{e,c}$, and constricted drag coefficient, $C_{D,c}$, can be defined as $R_{e,c} = R_e(u_c/u_p)$ and $C_{D,c} = C_D(u_p/u_c)^2$. For high values of K_C , Etmninan et al. (2019) propose that the two are related by the empirical expression:

$$C_{D,c} = 1 + 10R_{e,c}^{-2/3} \quad (20)$$

Figure 7 shows a comparison between the present data and Eq. (20). While there is some scatter, the results from the present isolated-cylinder and canopy experiments fall within approximately 10% of predicted values from Eq. (20), demonstrating that the equation can provide a good estimation of C_D in the absence of direct measurements. Nevertheless, in the present work, model calculations are based on measured C_D -values as shown in Fig. 6, taking the average measured values of $C_D = 1.30$ for the sparse canopy and $C_D = 2.30$ for the dense canopy.

It should be noted that most wave attenuation studies define an empirical “bulk drag coefficient” $C_{D,b}$, obtained from the measured wave attenuation using the method first described by Dalrymple et al. (1984). Henry et al. (2015) show examples of different $C_{D,b}$ formulations. In these studies, $C_{D,b}$ tends to decrease significantly with increasing R_e , because the calculation does not account for velocity reduction within the canopy (relative to the free-stream velocity), which increases with increasing R_e . In contrast, C_D in the present work is based directly on the incident in-canopy velocity, and, as Fig. 6 shows, C_D does not appear to vary significantly with R_e .

4 Results

4.1 Model validation

A comparison between the experimental results and the two analytical models is shown in Fig. 8 for all 10 cases. The measured free stream velocity is used to force the analytical models,

where the first three free stream harmonics are included in the nonlinear model and only the first harmonic in the sinusoidal model (Table 1). Based on the laboratory measurements, model calculations use $C_m = 1$, $C_D = 1.3$ for the sparse canopy and $C_D = 2.3$ for the dense canopy, while C_f is tuned for each case to achieve the best fit between the experimental data and the nonlinear model. The resulting non-dimensional quantities Γ_I , Γ_D and Γ_f are given in Table 1. It can be observed that the nonlinear model accurately captures both the phase, amplitude and overall temporal variation of the in-canopy velocity. The sinusoidal model is limited to a single harmonic ($M = 1$) and cannot reproduce the higher-order in-canopy velocity components, but it does accurately capture the phase and magnitude of the in-canopy velocity. The accuracy of the models is evaluated by calculating the normalized deviation to the experiments:

$$\delta = \frac{\|U - U_e\|_2}{\|U_e\|_2} \quad (21)$$

Here, U is the model prediction and U_e is the experimental data, with $\|\cdot\|_2$ denoting the 2-norm. The normalized deviations for the sinusoidal, nonlinear and Lowe et al. (2005) models, δ_S , δ_{NL} and δ_{LKM} , are provided in Table 1. The sinusoidal model shows differences between 10% and 16%, while the nonlinear and Lowe et al. (2005) models show better performance with differences between 4% and 11%. It is seen in Table 1 that the present nonlinear model generally results in smaller deviations from the experiments compared to the LKM model; however, this merely reflects that C_D and C_f are derived and tuned, respectively, to the present resistance formulation. The resistance formulation in Lowe et al. (2005) differs to the one proposed in the present work, which explains the small differences between δ_{NL} and δ_{LKM} . Identical results are obtained when applying the resistance formulation from Section 2.1 in both nonlinear models.

Figure 8 shows a comparison between measured velocities U and predictions obtained from sinusoidal and nonlinear models. Results from Lowe et al.’s (2005) time-domain model (henceforth LKM, 2005) are also shown in Fig. 8: there is practically no difference between the present nonlinear frequency domain model and LKM (2005), except for a small phase shift and difference in amplitude, which are attributed to the difference in canopy resistance formulation between the two nonlinear models.

The experimental data and nonlinear model predictions show a rapid flow acceleration followed by slow deceleration after the maximum velocity (Fig. 8). This is explained by the fact that the free stream velocity has its maximum at $t = 1.5$ s while the in-canopy velocity peaks much earlier, which means the external pressure gradient $\partial p/\partial x = -\rho \partial u_0/\partial t$ remains negative for some time after the maximum in-canopy velocity is reached, providing a forward driving force during this time.

Figure 9 shows the frequency composition of flow velocities for six representative cases (S1, S3, S5, D1, D3, and D5). The

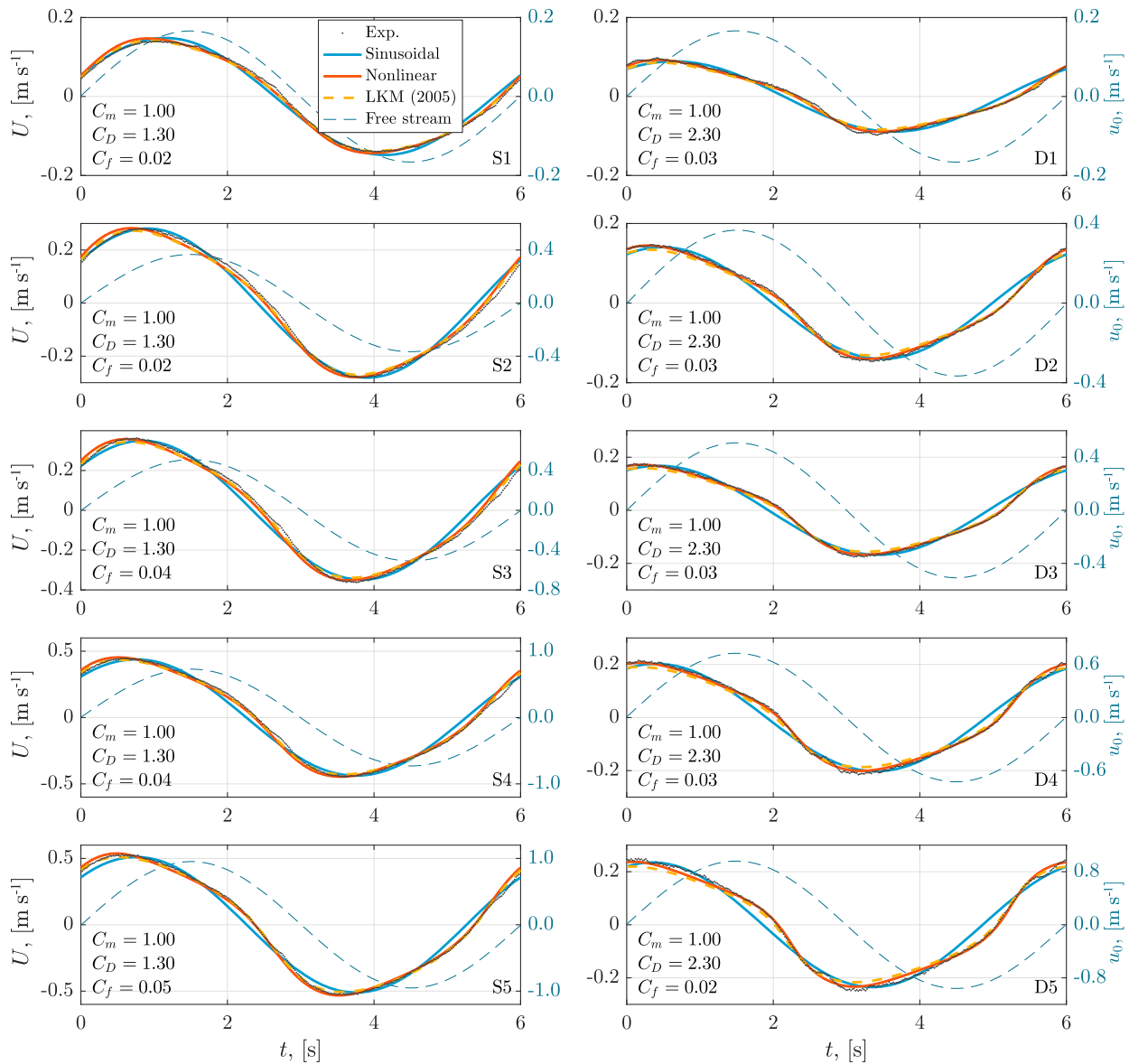


Figure 8 Comparison between the spatially-averaged in-canopy velocity, U , from experiments and predicted values from sinusoidal, nonlinear, and LKM (2005) models. The free stream velocity, u_0 , is shown with axis on the right of each panel. Left: Results for sparse canopy. Right: Results for dense canopy

figure shows the magnitude and phase of the 1st, 3rd and 5th harmonic of free-stream and in-canopy velocities for each case, together with model predictions obtained using the sinusoidal and nonlinear models, all normalized by the magnitude of the 1st harmonic of the free-stream velocity. Predictions obtained using LKM (2005) are also shown, and they are practically identical to the results from the nonlinear frequency-domain model. All three models predict the magnitude and phase of the 1st harmonic with relatively good accuracy. For each case, the figure shows that the free-stream velocity contains a 3rd harmonic with magnitude of between 1–5% of the first harmonic, while the 5th harmonic has a magnitude of $< 1\%$ of the 1st harmonic. The results demonstrate the nonlinearity introduced by the canopy, since for the first four cases shown, the 3rd harmonic of the in-canopy velocity is increased relative to the free-stream.

This nonlinearity is most pronounced for case S5, where the 1st harmonic reduces by $|U_1|/|u_1| \approx 0.6$ and the 3rd harmonic increases by $|U_3|/|u_3| \approx 2.5$. For the other two cases (D3 and D5), the 1st harmonic is significantly reduced ($|U_1|/|u_1| \leq 0.33$) while the 3rd harmonic remains near-constant. The canopy also introduces a 5th harmonic component with magnitude of between 0.5–2% of the 1st harmonic. In all cases, the nonlinear model, as well as LKM (2005), are shown to predict the magnitude and phase of the 3rd harmonic with good accuracy. The 5th harmonic is also approximated, albeit with less accuracy due to its small magnitude.

A comparison between the predicted (sinusoidal and nonlinear models) and measured velocity profiles is shown in Fig. 10. The two-layer models are found to capture the bulk behaviour accurately. The boundary layer formation on top of

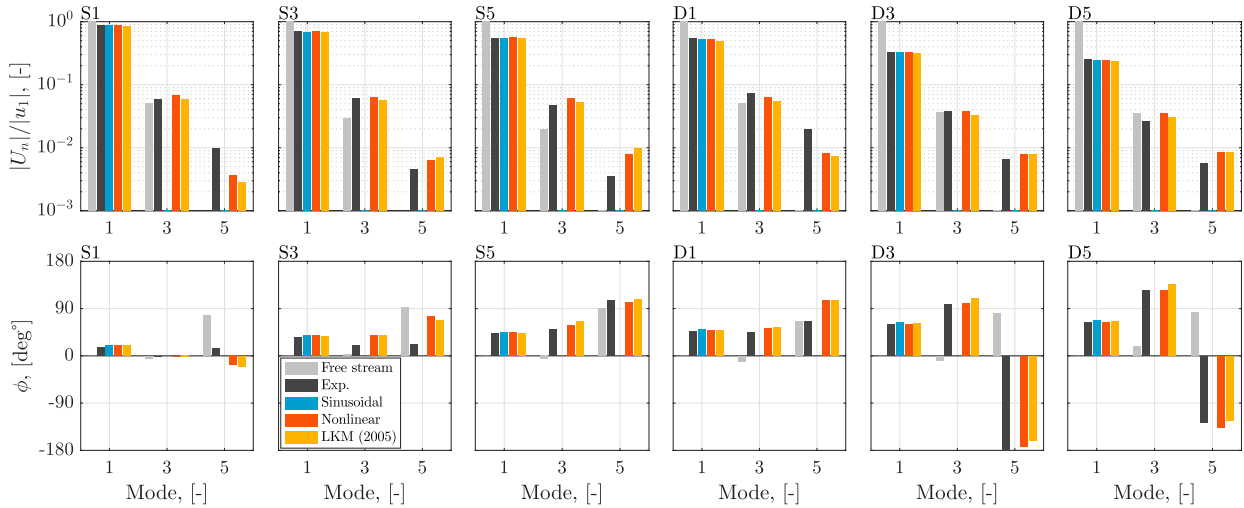


Figure 9 Comparison of the harmonic behaviour of the experimental results, sinusoidal, nonlinear, and LKM (2005) models. The label “Mode” refers to the $n = 1, 3, 5$ harmonics in the nonlinear models and experiments, and the $n = 1$ harmonic in the sinusoidal model. Top rows: The odd harmonic velocity magnitudes $|U_1|$, $|U_3|$, and $|U_5|$. Bottom rows: The odd phases relative to the first harmonic free stream phase: $\phi_n = \arg U_n - \arg u_1$ for $n = 1, 3, 5$

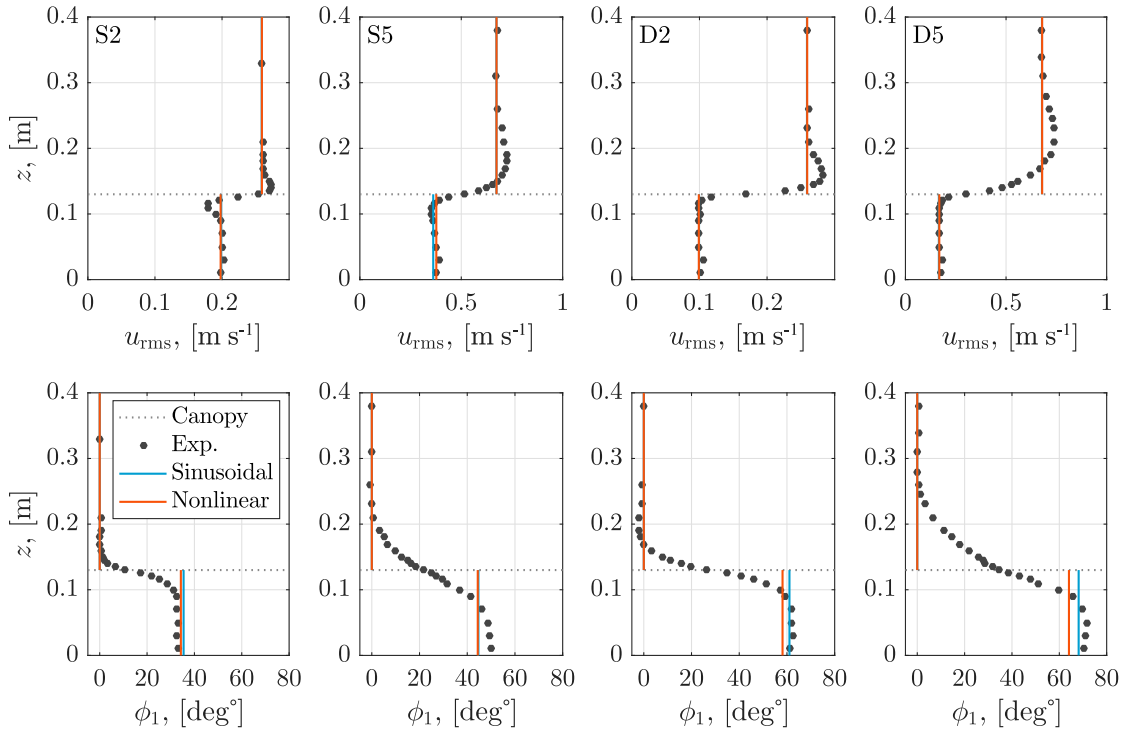


Figure 10 Measured and predicted vertical velocity profiles. Top panels: Root-mean-square velocity, u_{rms} . Bottom panels: Phase difference between in-canopy and free stream velocities based on the first harmonic only

the canopy is not captured, as this would require a higher vertical resolution (e.g. Chen & Zou, 2019; Zeller et al., 2015). The velocity in the canopy leads over the free stream velocity (bottom panels) and the sinusoidal and nonlinear models both predict almost identical phase leads ($\phi_1 = \arg U_1 - \arg u_1$) with good match to the measurements. The experimental measurements did not resolve the wave boundary layer at the bottom of the flow tunnel, though it is hypothesized that the phase lead will further increase towards the bed akin to observations from laminar and turbulent wave boundary layers over smooth and

rough beds (Jensen et al., 1989). It is furthermore hypothesized that the additional phase lead will be smaller than that for undisturbed wave boundary layers, because the canopy has already introduced a phase lead with respect to the external pressure gradient. These hypotheses should be addressed experimentally and theoretically, as they might prove important for a description of in-canopy sediment transport. The accuracy of the nonlinear model in terms of predicting the phase lead, momentum distribution, and in-canopy velocity reduction factors is incorporated in the results presented in Sections 4.2–4.4.

4.2 Comparison between sinusoidal and nonlinear drag models

In this section, we compare sinusoidal and nonlinear model predictions of in-canopy flow for a wide range of conditions: $n = [0.9, 0.999]$, $d = 0.01$ m, $T \in [2, 16]$ s, $|u_1| \in [0.01, 2.0]$ m s⁻¹, $C_m = \{1, 2\}$, $C_d = \{1, 2\}$, and $C_f = \{0, 0.02\}$. The comparison is done for 4700 conditions in total. In all cases, the free-stream velocity is purely sinusoidal ($u_m = 0$ for $m = 2, 3, \dots$). Two assessment measures are used in the comparison: (i) magnitude of the first harmonic, and (ii) the phase between u_1 and U_1 .

The magnitude of the first harmonic \hat{U}_1 was found to be within $\pm 5\%$ of each other for all cases (not shown). This is of considerable practical importance, because it suggests that the linearization applied in free surface models is sufficiently accurate (e.g. Jacobsen, 2016; Méndez et al., 1999). It could be that the vertical velocity component in the case of real waves influences the accuracy of the sinusoidal model; however, in the absence of a valid nonlinear wave theory for canopies, it seems to be a good engineering approximation to apply a wave theory based on a linearized drag force.

The phase lead in the oscillatory flow case has limited direct physical implications; however, for real waves the vertical distribution of the phase lead between the horizontal and vertical velocities is important for residual wave-induced stresses (Deigaard, 1993; Deigaard & Fredsøe, 1989; Guannel & Özkan-Haller, 2014; Jacobsen, 2016; Jacobsen & McFall, 2022; Philips, 1980). Since there is no nonlinear free surface wave theory for canopies, the oscillatory solution is used to assess the implications of using a linearized wave theory to calculate period-averaged wave stresses. The two analytical models, with $C_f = 0.0$, are compared in Fig. 11 (top panel) and it is seen that there are some differences between the two. However, the differences are small (less than 3°) and are seen only at high Γ_D for which the phase lead is already considerable (greater than 45°).

Figure 11 (bottom panel) shows the phase leads predicted by the two models with $C_f = 0.02$. It is seen that the models predict lower phase leads for $C_f = 0.02$ compared to $C_f = 0.00$. Furthermore, for large values of Γ_D , the results for $C_f = 0.02$ show decreasing phase lead with increasing Γ_D , which is attributed to the increasing importance of Γ_f for large in-canopy velocity. For $\Gamma_D > 2$, the predicted phase leads branch off and the different branches are found to coincide with constant values of NC_D , where the lowest branches correspond to small values of NC_D and the highest branches to large values of NC_D . The branching off therefore relates to the relative importance of friction versus in-canopy drag. The experimental phase leads are included in Fig. 11 and are seen to align better with the model predictions for $C_f = 0.02$ than for $C_f = 0.0$. The importance of C_f on the in-canopy velocity reduction is addressed below. For the remainder of the work, only the nonlinear model is applied.

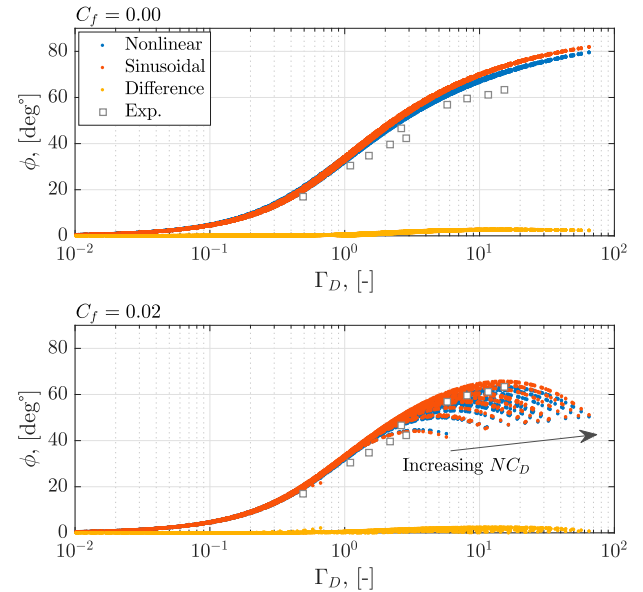


Figure 11 Comparison of the $\arg U_1$ relative to $\arg u_1 = 0$ for the sinusoidal and nonlinear models. Top: $C_f = 0.00$. Bottom: $C_f = 0.02$. The range of NC_D is 13–2546

4.3 In-canopy frequency distribution and momentum exchange

It was discussed in Section 2.3 that the products $|U|U$ and $|\Delta U|\Delta U$ give rise to an exchange of momentum between the harmonics for the nonlinear model. The relative magnitude of the in-canopy harmonics $|U_m|/|U_1|$ for $m = 2, 3, 4, 5$ is depicted in Fig. 12 as a function of Γ_D and the free stream magnitude of the second harmonic $|u_2|/|u_1| = \{0.00, 0.125, 0.25\}$. The extension of the simulations from Section 4.2 to now include $|u_2|/|u_1| > 0$ is to consider the effect of finite wave heights and Stokes second-order type phenomena (Svendsen & Jonsson, 1982), which leads to skewed free stream velocity signals. The free stream velocity signal has a secondary bump in the trough of the velocity signal for $|u_2|/|u_1| > 0.25$, which is non-physical for a regular wave signal.

Results obtained for $C_f = 0.0$ in Fig. 12 (all panels) collapse well when plotted against Γ_D , demonstrating that Γ_D is an appropriate descriptive parameter for the higher harmonic content of the in-canopy velocity. The results for $C_f = 0.02$ and $|u_2|/|u_1| = 0$ exhibit the same branching as seen for the phase lead, whereby branches correspond to different values of NC_D . The experimental data are also shown (top panel) and there is reasonable correspondence with the model results. However, the experimental ratio for $|U_3|/|U_1|$ is larger than the model ratio. This is explained by the presence of small amounts of higher harmonic content in the measured free stream velocity (Table 1), e.g. $|u_3|/|u_1| \simeq 5\%$ for case D1, which is the “outlier” in Fig. 12. There is an overall good match between model and experiments for $|U_3|/|U_1|$. It is furthermore seen that $|U_3|/|U_1|$ becomes larger when friction is introduced ($C_f = 0.02$) and Γ_D is not the sole descriptive parameter for the momentum exchange between

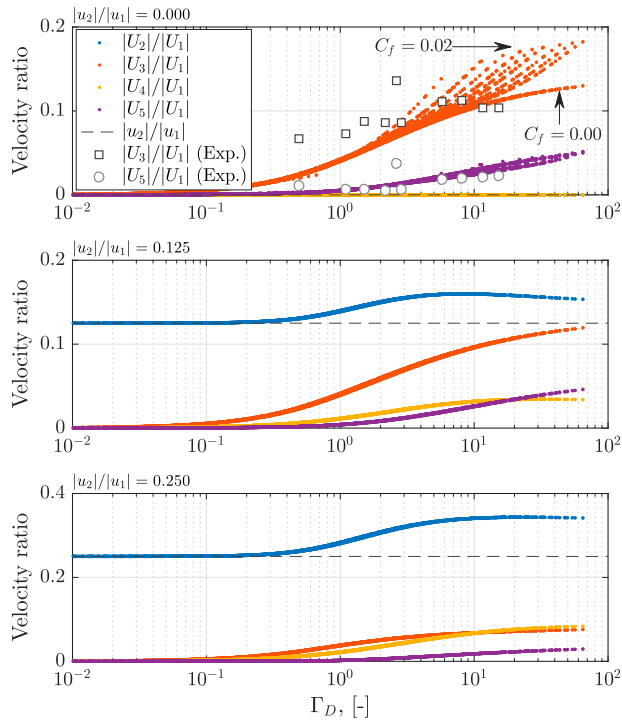


Figure 12 In-canopy velocity amplitudes $|U_m|/|U_1|$ for $m = 2, 3, 4, 5$ predicted by the nonlinear model. Top: $|u_2|/|u_1| = 0$. $C_f = \{0.00, 0.02\}$. Middle: $|u_2|/|u_1| = 0.125$ and $C_f = 0.00$. Bottom: $|u_2|/|u_1| = 0.25$ and $C_f = 0.00$. The experimental data are inserted in the top panel

harmonics. The effect of C_f on the bulk velocity reduction is treated in Section 4.4.

For the velocity-skewed cases (middle and bottom panels) it can be seen that $|U_2|/|U_1| \geq |u_2|/|u_1|$ and that the introduction of free stream momentum content on u_2 suppresses the relative momentum content on the odd harmonics ($|U_m|/|U_1|$ for $m = 3, 5, \dots$). Furthermore, for the simulations with $|u_2|/|u_1| = 0.25$, $|U_2|/|U_1| \geq 0.25$, which means that a secondary bump is encountered in the in-canopy velocity signal. Examples of velocity time-series for $\Gamma_D = \{0.1, 1.0, 10.0\}$ and $|u_2|/|u_1| = \{0.00, 0.125, 0.25\}$ are shown in Fig. 13, where the secondary bump can be seen in the bottom panel. The free stream velocity signals in the middle and bottom panels are velocity-skewed, though the in-canopy velocity signal becomes increasingly asymmetric (sawtooth-shaped) for increasing Γ_D and $|u_2|/|u_1|$. The influence of the time variation in U on sediment transport is discussed in Section 5.3.

The importance of the sub-harmonic contributions is depicted in Fig. 14, where the sum of self-induced and super-harmonic contributions are shown as solid markers and the sub-harmonic contributions are shown as open markers. For $|u_2|/|u_1| = 0$ (top panel), it is seen that the sub-harmonic contributions are small for $m = 1$ for all values of Γ_D , while for $m = 3$ the sub-harmonic contributions are 10% or more relative to the self-induced and super-harmonic contributions for $\Gamma_D > 10$. Introduction of a velocity-skewed free stream velocity ($|u_2|/|u_1| = 0.25$, bottom panel) shows that the distribution

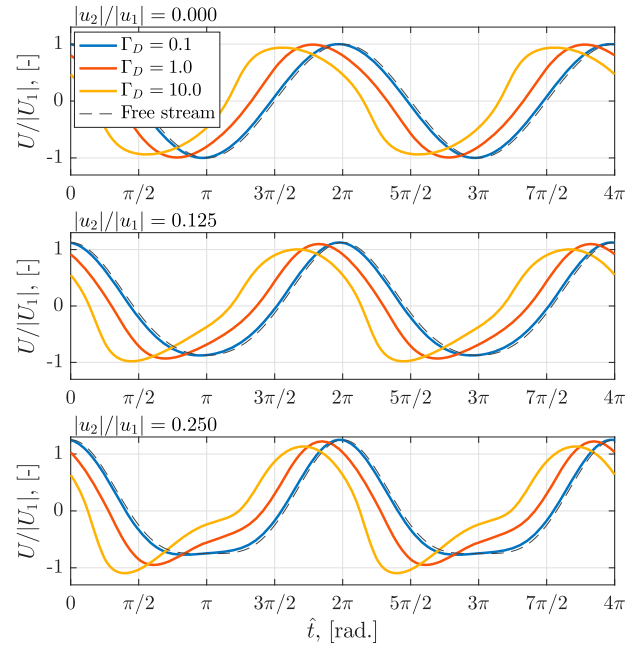


Figure 13 The velocity time-series for three values of $\Gamma_D = \{0.1, 1, 10\}$ and the associated free stream velocity for nonlinear model results. Top: $|u_2|/|u_1| = 0$. Middle: $|u_2|/|u_1| = 0.125$. Bottom: $|u_2|/|u_1| = 0.25$

is practically unaltered for $m = 3$ and that the sub-harmonic contributions are small for $m = 2$. For $m = 1$ the sub-harmonic contribution exceeds 10% for $\Gamma_D > 1$. The importance of sub-harmonic momentum on $m = 1$ is relevant to consider, if a solution to nonlinear, free surface waves in canopies is sought: Any nonlinear wave will have significant velocity-skewness, so the relative importance of drag contributions will have more resemblance to the bottom panel than to the top panel and sub-harmonic contributions may not be negligible.

The existence of higher in-canopy harmonics (even for $u_m = 0$, $m = 2, 3, \dots$) means that there must be a shear transfer of higher harmonic velocities into the free stream, since there is otherwise no momentum balance at the canopy interface. This higher harmonic shear component could be a source for eddy viscosity generation and shear layer instabilities in the wave boundary layer on top of the canopy.

4.4 In-canopy velocity reduction

Lowe et al. (2005) presented a solution for, and qualitative discussion of, the in-canopy velocity reduction. However, they considered two independent nondimensional quantities (d/S and a_1/S) instead of their product: $\Gamma_D \propto (d/S) \cdot (a_1/S)$. All the results from the nonlinear computations above are presented as the ratio $\max \hat{U} / \max \hat{u}_0$ in Fig. 15 (top panel), where it is important to note that the use of \hat{U} and \hat{u}_0 includes all higher-order velocity components. Overall, there is limited scatter in $\max \hat{U} / \max \hat{u}_0$ at given Γ_D , except for small Γ_D (inertia-dominated flow). The scatter for small Γ_D follows directly from the momentum equation, which reads as follows for vanishing

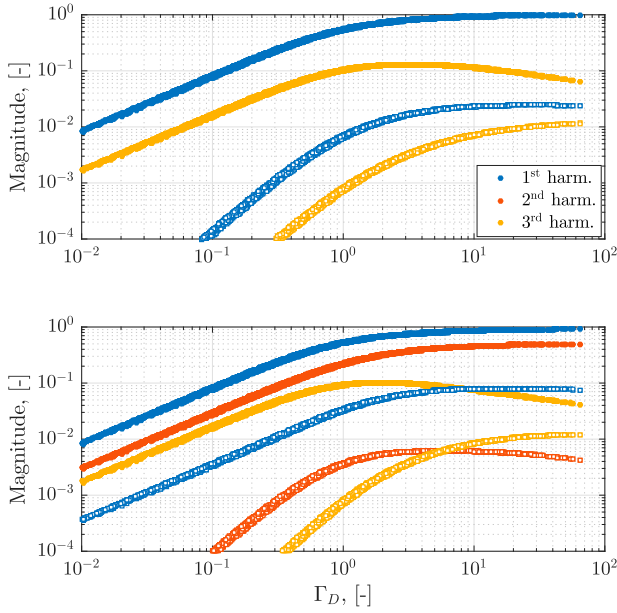


Figure 14 The drag contributions to the first three harmonics, where solid markers are the combination of self-induced and super-harmonic drag and open markers are the sub-harmonic drag. Top: $|u_2|/|u_1| = 0$. Bottom: $|u_2|/|u_1| = 0.25$

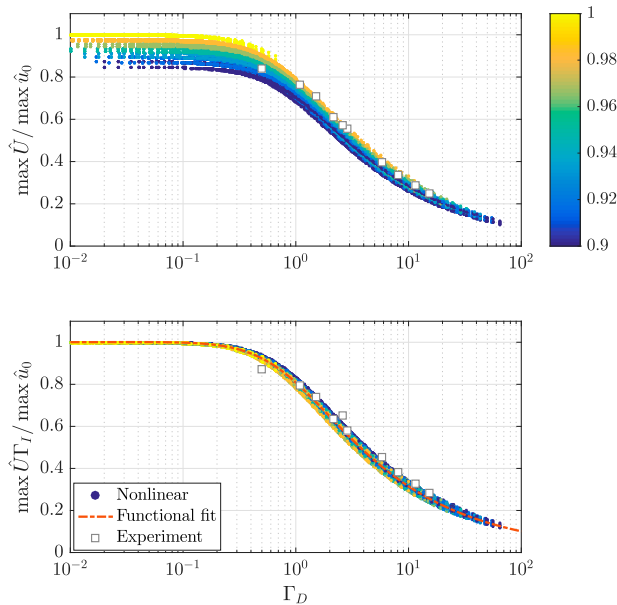


Figure 15 In-canopy velocity reduction as a function of Γ_D . Top: $\max \hat{U} / \max \hat{u}_0$. Bottom: $\max \hat{U} \Gamma_I^{-1} / \max \hat{u}_0$. The colourbar shows n . The functional fit in the bottom panel is given by Eq. (23)

drag:

$$\frac{\partial \hat{U}}{\partial t} = \frac{1}{\Gamma_I} \frac{\partial \hat{u}_0}{\partial t} \rightarrow \hat{U} = \frac{\hat{u}_0}{\Gamma_I} \quad (22)$$

This gives a minimum inertia-related velocity reduction by $\Gamma_I^{-1} < 1$, which is incorporated in the bottom panel, where the ratio $\max \hat{U} \Gamma_I^{-1} / \max \hat{u}_0$ is shown to be a function of Γ_D only. Note that the figure contains data for both $C_f = 0.00$ and $C_f = 0.02$, so the friction on top of the canopy has no noticeable

effect on the velocity reduction, which is contrary to the findings for the phase lead and momentum distribution on individual harmonics. The bottom panel shows that when normalized by the minimum inertia-related velocity reduction, Γ_D is the sole nondimensional parameter that determines the velocity reduction. Figure 15 also contains the experimental data and there is a good match from inertia- to drag-dominated regimes.

Based on these results, an analytical expression is presented that can be used for an engineering estimate of the in-canopy velocities for regular, oscillatory flows:

$$\frac{\max \hat{U}}{\max \hat{u}_0} \simeq \frac{1}{\Gamma_I} \sqrt{\frac{1 + 1.40\Gamma_D}{1 + 1.30\Gamma_D + 1.37\Gamma_D^2}} \quad (23)$$

This function is valid for horizontal, oscillatory free stream flows with a first and second harmonic content, where the two harmonics are in phase, and $|u_2|/|u_1| \leq 0.25$. It is furthermore valid for $0.9 \leq n$ and $0.00 \leq C_f \leq 0.02$. It remains to be shown whether this expression can be used for the prediction of in-canopy velocities for real waves with a considerable vertical velocity component. The inertia-related velocity reduction (Γ_I^{-1}) on the left-hand side is reasonably estimated by setting $C_m = 1$ for large Keulegan–Carpenter numbers (Sumer & Fredsøe, 1999). It is also found that:

$$\frac{\max \hat{U}}{\max \hat{u}_0} \simeq \frac{\hat{U}_{rms}}{\hat{u}_{0,rms}} \quad (24)$$

following the same functional fit. This is a relaxation (use of “ \simeq ”) of the exact identity for purely sinusoidal motion for which $\max \hat{U} = \sqrt{2} \hat{U}_{rms}$ and $\max \hat{u}_0 = \sqrt{2} \hat{u}_{0,rms}$.

5 Perspective and implications

5.1 Development of higher-order free surface wave theory

Analytical models of dissipative, free surface waves in canopies are found in the literature and they are all restricted to first order with a linearized drag formulation (Asano et al., 1992; Dubi & Tørum, 1994; Jacobsen, 2016; Kobayashi et al., 1993; Méndez et al., 1999), i.e. with a sinusoidal time variation of all variables. The present analysis has shown that accurate results should be expected from linear wave theories with respect to the in-canopy velocity, so the estimated radiation stress tensors (Jacobsen, 2016; Mendez et al., 1998), Lagrangian Stokes drift (Jacobsen, 2016), and vertical shear stress distribution (Jacobsen & McFall, 2022) should be reasonably approximated and can be applied in large-scale, practical engineering models, which rely on the second-order terms from Airy wave theory.

However, for waves in non-vegetated, shallow water with high nonlinearity, the use of linear wave theory breaks down for the horizontal momentum flux, which was illustrated quantitatively by Dean and Bender (2006), so development of a higher-order wave theory for in-canopy wave propagation is

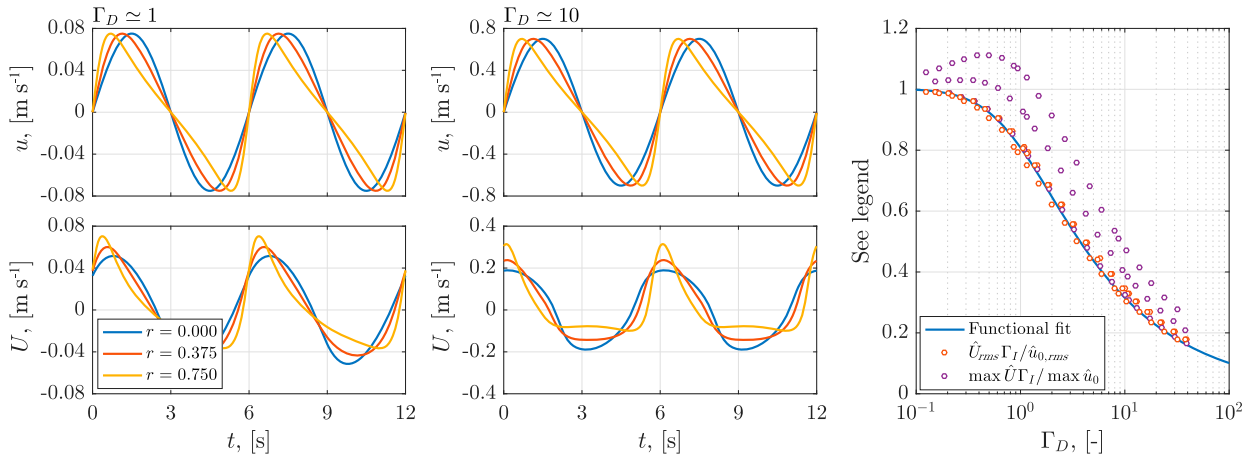


Figure 16 Velocity-asymmetric free stream velocity. Left column: maximum free stream velocity of 0.075 m s^{-1} and varying $r = \{0, 0.375, 0.75\}$. Middle column: same as left with maximum free stream velocity of 0.70 m s^{-1} . Right column: fit with Eq. (23) for ratio of maximum velocities and ratio of standard deviations, respectively

needed for special applications. The present analysis suggests that there is limited gain in developing a second-order free surface wave theory, because the theory would still rely on a linearized drag (no third-order contributions proportional to e.g. $B_1 U_2$, $B_2 U_1$). Secondly, the present analysis indicates that a higher-order wave theory ought not to be based on a perturbation approach, but rather on a direct solution of the closure coefficients, as done with stream function wave theory (Fenton, 1988; Rienecker & Fenton, 1981), because the sub-harmonic contributions may not be negligible to the first harmonic and thus invalidate a perturbation approach for large values of Γ_D .

5.2 Velocity-asymmetric free stream velocity

The bulk of this work investigated velocity-skewed free stream velocities, so here the transformation of a velocity-asymmetric free stream velocity into a canopy is briefly presented. The free stream velocity by Abreu et al. (2010) is applied:

$$u_0 = u_w \sqrt{1 - r^2} \frac{\sin \omega t + r \sin \varphi / (1 + \sqrt{1 - r^2})}{1 - r \cos(\omega t + \varphi)} \quad (25)$$

where $0 \leq r \leq 0.75$ gives the degree of velocity-asymmetry for $\varphi = 0$, and $u_w = (\max u_0 - \min u_0)/2$. u_0 is decomposed as per Eq. (8) and the harmonic amplitudes are given as input to the nonlinear frequency-domain model. Examples with $u_w = \{0.075, 0.70\} \text{ m s}^{-1}$, $N = 1736 \text{ stems m}^{-2}$, $d = 0.0083 \text{ m}$, $C_m = 1$, $C_D = 2.3$, $T = 6.0 \text{ s}$, and $r = \{0, 0.375, 0.75\}$ are shown in Fig. 16. It is seen that there is a significant difference between the positive and negative part of U and qualitatively it is concluded that U becomes increasingly velocity-skewed for increasing r (increasing free stream velocity asymmetry). This holds both for $\Gamma_D \approx 1$ and $\Gamma_D \approx 10$. Here, “ \approx ” is applied, since $|u_i|$ varies with r for a fixed u_w .

U was computed for a range of $u_w \in [0.01, 2.5] \text{ m s}^{-1}$ and the two forms of the velocity reduction $\hat{U}_{rms} \Gamma_I / \hat{u}_{0,rms}$ and $\max \hat{U} \Gamma_I / \max \hat{u}_0$ are depicted against Eq. (23) in Fig. 16

(right panel). It can be seen that only the form based on the rms-velocities collapses with the functional fit.

5.3 Sediment transport

Sediment transport within canopies under oscillating flow and waves has been reported in a few studies (Tinoco & Coco, 2014, 2018; Yang et al., 2016), who report that the sediment transport is linked to the in-canopy turbulent kinetic energy. Yang et al. (2016) found that the critical velocity within the canopy for incipient sediment transport decreased with decreasing porosity (increasing solidity), while the critical turbulence level was estimated to be constant. Furthermore, Tinoco and Coco (2018) measured suspended sediment concentrations and showed positive correlations between sediment concentrations, turbulence levels and solidity.

Nakayama and Kuwahara (1999), Yang et al. (2016) and Tinoco and Coco (2018) proposed formulations for turbulent kinetic energy in repeated arrays that are proportional to the square of the in-canopy velocity, with the proportionality factor depending on the porosity (solidity). A combination of the proposed empirical formula for the in-canopy velocity (Eq. (23)) and the work by Nakayama and Kuwahara (1999) can be used to predict in-canopy turbulent kinetic energy, though validation against experimental data is required for a validated, predictive formulation. A validated model would allow for a prediction of the in-canopy suspended sediment concentrations based on Γ_D and Γ_I as sole input parameters along with the characteristics of the sediment (density and median diameter).

The in-canopy redistribution of momentum to higher harmonics may be important in determining period-averaged (net) sediment flux, which is required for practical engineering applications. It is documented for non-vegetation wave boundary layers that the direction of net sediment transport under nonlinear free stream velocities depends on the sediment fall velocity and the velocity asymmetry and skewness (Fuhrman et al., 2013;

Hassan & Ribberink, 2005; O'Donoghue & Wright, 2004). Coarse sediment is found to have a net transport in the direction of wave propagation, while the net transport of finer sediment can be in the opposite direction. This effect is expected to be more pronounced for vegetated wave boundary layers, because the stem drag introduces higher-order modes within the canopy, even for sinusoidal free-stream flow.

6 Conclusion

Two frequency-domain models for the bulk in-canopy velocity under oscillatory flow have been presented, one in which the drag due to the canopy depends nonlinearly on the flow velocity and one in which the drag is linearized (called the sinusoidal model). For the former, the super- and sub-harmonic mechanisms of momentum transfer between frequencies are quantified. The models have been validated against new experimental data from an oscillatory flow tunnel for unprecedented large-amplitude free-stream velocities up to 1.00 m s^{-1} . The nonlinear model is seen to capture the higher-harmonic momentum generation by the vegetation.

A direct comparison between the sinusoidal and nonlinear model predictions of in-canopy velocity magnitudes and phase leads show minor differences between the two models. From this, it is inferred that linearized free surface wave models provide reasonable accuracy, when it comes to the quantification of radiation stresses, vertical shear stress distribution, and Stokes drift for application in large-scale, practical engineering models.

The momentum transfer between harmonics is described and it is seen that it is a function of one non-dimensional parameter: Γ_D . It is also seen that sub-harmonics are of considerable importance for large values of Γ_D and high free-stream nonlinearity. This means that a perturbation approach for a nonlinear free surface model will not account correctly for all in-canopy momentum transfer between harmonics.

Finally, it was found that Γ_I and Γ_D are determining factors for in-canopy velocities. Normalization of the in-canopy velocity by Γ_I unified all velocity reduction factors onto a single fitting line (Eq. (23)), which shows good agreement with the experimental data and it is applicable to both velocity-skewed and velocity-asymmetric free stream velocities.

Notation

$\hat{}$	= non-dimensionalised term
*	= complex conjugate
a_1	= 1st harmonic of free stream orbital amplitude (m)
b_i	= i 'th Fourier component of $ \Delta U $ (–)
B_i	= i 'th Fourier component of $ U $ (–)
C_D	= drag coefficient (–)
$C_{D,b}$	= bulk drag coefficient (–)
$C_{D,c}$	= constricted drag coefficient (–)
C_f	= friction coefficient (–)

C_m	= added mass coefficient (–)
d	= stem diameter (m)
F_D	= fluid drag per unit mass (m s^{-2})
h_v	= canopy height (m)
K_C	= Keulegan-Carpenter number (–)
M	= size of matrix system (–)
M_y	= moment applied to load cell ($\text{kg m}^2 \text{ s}^{-2}$)
N	= stems per unit area (m^{-2})
N_w, N_a	= number of measuring points within and above canopy (–)
n	= porosity (–)
$P(n)$	= stem geometry parameter (–)
p	= pressure (Pa)
r	= Abreu et al. (2010) skewness parameter (–)
\mathbf{R}_e	= Reynolds number (–)
$\mathbf{R}_{e,c}$	= constricted Reynolds number (–)
S	= generic measure for stem spacing (m)
S_x, S_y	= stem centre-to-centre spacing along x, y (m)
T	= oscillatory flow period (s)
t	= time (s)
u, v, w	= velocity components along x, y, z (m s^{-1})
$u_0(t)$	= free stream velocity (m s^{-1})
u_i	= i 'th harmonic of u_0 (m s^{-1})
u_c	= constricted velocity (m s^{-1})
u_{rms}	= root-mean-square of u_0 (m s^{-1})
u_w	= Abreu et al. (2010) velocity height (m s^{-1})
$U(t)$	= bulk in-canopy filter velocity (m s^{-1})
U_{rms}	= root-mean-square of U (m s^{-1})
$\Delta U(t)$	= velocity difference (m s^{-1})
$u_e(z, t)$	= experimentally measured velocity (m s^{-1})
u_p	= pore velocity (m s^{-1})
U_i	= i 'th harmonic of U (m s^{-1})
x, y, z	= spatial coordinates (m)
Γ_D	= non-dimensional drag term (–)
Γ_f	= non-dimensional friction term (–)
Γ_I	= non-dimensional inertia term (–)
$\Gamma_{L,D}$	= linearised drag term (–)
$\Gamma_{L,f}$	= linearised friction term (–)
α_U	= shape factor for in-canopy velocity profile (–)
δ	= normalised measurement deviation (–)
λ	= solidity (–)
ν	= kinematic viscosity ($\text{m}^2 \text{ s}^{-1}$)
ν_t	= eddy viscosity ($\text{m}^2 \text{ s}^{-1}$)
ρ	= fluid density (kg m^{-3})
ϕ_i	= i 'th component of the phase lag (rad)
φ	= Abreu et al. (2010) waveform parameter (–)
ω	= cyclic frequency (s^{-1})

Note

- Note that this choice of characteristic parameters is consistent with Jacobsen, Bakker, et al. (2019); see their Section 3.1 for a discussion.

Acknowledgments

ON acknowledges funding from the University of Aberdeen to support his PhD. The authors acknowledge the support of the University of Aberdeen technical staff for the experimental work, especially that of Fluids Laboratory Technician Roy Gillanders. The experimental dataset is available on <https://dx.doi.org/10.5281/zenodo.4560141>.

Disclosure statement

No potential conflict of interest was reported by the author(s).

ORCID

Otto E. Neshamar  <http://orcid.org/0000-0001-5673-6293>
 Niels G. Jacobsen  <http://orcid.org/0000-0003-2662-6282>
 Dominic A. Van Der A  <http://orcid.org/0000-0003-1025-9465>
 Tom O'Donoghue  <http://orcid.org/0000-0002-7843-1340>

References

- Abreu, T., Silva, P. A., Sancho, F., & Temperville, A. (2010). Analytical approximate wave form for asymmetric waves. *Coastal Engineering*, 57, 656–667. <https://doi.org/10.1016/j.coastaleng.2010.02.005>
- Anderson, M. E., & Smith, J. M. (2014). Wave attenuation by flexible, idealized salt marsh vegetation. *Coastal Engineering*, 83, 82–92. <https://doi.org/10.1016/j.coastaleng.2013.10.004>
- Asano, T., Deguchi, H., & Kobayashi, N. (1992). Interaction between water waves and vegetation. *Proceeding to Coastal Engineering Conference, VI*, 2710–2723. <https://doi.org/10.1061/9780872629332.206>
- Bridges, T. S., Smith, J. M., King, J. K., Simm, J. D., Dillard, M., deVries, J., Reed, D., Piercy, C. D., van Zanten, B., Arkema, K., Swannack, T., H. de Looft, Lodder, Q., Jeuken, C., Ponte, N., Gailani, J. Z., Whitfield, P., Murphy, E., Lowe, R. J., ... Naylor, L. A. (2022). Coastal natural and nature-based features: International guidelines for flood risk management. *Frontiers in Built Environment*, 8, 1–9. <https://doi.org/10.3389/fbuil.2022.904483>
- Cao, H., Feng, W., Hu, Z., Suzuki, T., & Stive, M. J. F. (2015). Numerical modeling of vegetation-induced dissipation using an extended mild-slope equation. *Ocean Engineering*, 110, 258–269. <https://doi.org/10.1016/j.oceaneng.2015.09.057>
- Chen, H., & Zou, Q.-P. (2019). Eulerian-Lagrangian flow-vegetation interaction model using immersed boundary method and OpenFOAM. *Advances in Water Resources*, 126, 176–192. <https://doi.org/10.1016/j.advwatres.2019.02.006>
- CISL (2022). *Decision-making in a nature positive world: A corporate diagnostic tool to advance organisational understanding of nature-based solutions projects and accelerate their adoption*. The University of Cambridge Institute for Sustainability Leadership.
- Dalrymple, R. A., Kirby, J. T., & Hwang, P. A. (1984). Wave diffraction due to areas of energy dissipation. *Journal of Waterway, Port, Coastal and Ocean Engineering*, 110(1), 67–79. [https://doi.org/10.1061/\(ASCE\)0733-950X\(1984\)110:1\(67\)](https://doi.org/10.1061/(ASCE)0733-950X(1984)110:1(67))
- Dean, R. G., & Bender, C. J. (2006). Static wave setup with emphasis on damping effects by vegetation and bottom friction. *Coastal Engineering*, 53(2-3), 149–156. <https://doi.org/10.1016/j.coastaleng.2005.10.005>
- Deigaard, R. (1993). A note on the 3-dimensional shear-stress distribution in a surf zone. *Coastal Engineering*, 20(1-2), 157–171. [https://doi.org/10.1016/0378-3839\(93\)90059-H](https://doi.org/10.1016/0378-3839(93)90059-H)
- Deigaard, R., & Fredsøe, J. (1989). Shear-stress distribution in dissipative water-waves. *Coastal Engineering*, 13(4), 357–378. [https://doi.org/10.1016/0378-3839\(89\)90042-2](https://doi.org/10.1016/0378-3839(89)90042-2)
- Dubi, A., & Tørum, A. (1994). Wave damping by kelp vegetation. *Proceeding to Coastal Engineering Conference, I*, 142–156. <https://doi.org/10.1061/9780784400890.012>
- Etminan, V., Lowe, R. J., & Ghisalberti, M. (2019). Canopy resistance on oscillatory flows. *Coastal Engineering*, 152, 103502. <https://doi.org/10.1016/j.coastaleng.2019.04.014>
- Fenton, J. D. (1988). The numerical-solution of steady water-wave problems. *Computers & Geosciences*, 14(3), 357–368. [https://doi.org/10.1016/0098-3004\(88\)90066-0](https://doi.org/10.1016/0098-3004(88)90066-0)
- Fuhrman, D. R., Schløer, S., & Sterner, J. (2013). RANS-based simulation of turbulent wave boundary layer and sheet-flow sediment transport processes. *Coastal Engineering*, 73, 151–166. <https://doi.org/10.1016/j.coastaleng.2012.11.001>
- Guannel, G., & Özkan-Haller, H. T. (2014). Formulation of the undertow using linear wave theory. *Physics of Fluids*, 26(5), 1–18. <https://doi.org/10.1063/1.4872160>
- Hassan, W. N., & Ribberink, J. S. (2005). Transport processes of uniform and mixed sands in oscillatory sheet flow. *Coastal Engineering*, 52(9), 745–770. <https://doi.org/10.1016/j.coastaleng.2005.06.002>
- He, F., Chen, J., & Jiang, C. (2019). Surface wave attenuation by vegetation with the stem, root and canopy. *Coastal Engineering*, 152, Article 103509, 1–12. <https://doi.org/10.1016/j.coastaleng.2019.103509>
- Henry, P.-Y., Myrhaug, D., & Aberle, J. (2015). Drag forces on aquatic plants in nonlinear random waves plus current. *Estuarine, Coastal and Shelf Science*, 165, 10–24. <https://doi.org/10.1016/j.ecss.2015.08.021>
- Jacobsen, N. G. (2016). Wave-averaged properties in a submerged canopy: Energy density, energy flux, radiation stresses and Stokes drift. *Coastal Engineering*, 117, 57–69. <https://doi.org/10.1016/j.coastaleng.2016.07.009>
- Jacobsen, N. G., Bakker, W., Uijtewaal, W. S. J., & Uitenbogaard, R. (2019). Experimental investigation of the

- wave-induced motion of and force distribution along a flexible stem. *Journal of Fluid Mechanics*, 880, 1036–1069. <https://doi.org/10.1017/jfm.2019.739>
- Jacobsen, N. G., & McFall, B. C. (2022). Wave-averaged properties for non-breaking waves in a canopy: Viscous boundary layer and vertical shear stress distribution. *Coastal Engineering*, 174, Article 104117, 15 pages. <https://doi.org/10.1016/j.coastaleng.2022.104117>
- Jacobsen, N. G., McFall, B. C., & Van der A, D. A. (2019). A frequency distributed dissipation model for canopies. *Coastal Engineering*, 150, 135–146. <https://doi.org/10.1016/j.coastaleng.2019.04.007>
- Jadhav, R. S., Chen, Q., & Smith, J. M. (2013). Spectral distribution of wave energy dissipation by salt marsh vegetation. *Coastal Engineering*, 77, 99–107. <https://doi.org/10.1016/j.coastaleng.2013.02.013>
- Jensen, B., Jacobsen, N. G., & Christensen, E. D. (2014). Investigations on the porous media equations and resistance coefficients for coastal structures. *Coastal Engineering*, 84, 56–72. <https://doi.org/10.1016/j.coastaleng.2013.11.004>
- Jensen, B. L., Sumer, B. M., & Fredsøe, J. (1989). Turbulent oscillatory boundary-layers at high Reynolds-numbers. *Journal of Fluid Mechanics*, 206, 265–297. <https://doi.org/10.1017/S0022112089002302>
- Jordan, P., & Fröhle, P. (2022). Bridging the gap between coastal engineering and nature conservation? *Journal of Coastal Conservation*, 26, 4. <https://doi.org/10.1007/s11852-021-00848-x>
- Kobayashi, N., Raichle, A. W., & Asano, T. (1993). Wave attenuation by vegetation. *Journal of Waterway, Port, Coastal and Ocean Engineering*, 119(1), 30–48. [https://doi.org/10.1061/\(ASCE\)0733-950X\(1993\)119:1\(30\)](https://doi.org/10.1061/(ASCE)0733-950X(1993)119:1(30))
- Lowe, R. J., Koseff, J. R., & Monismith, S. G. (2005). Oscillatory flow through submerged canopies: 1. Velocity structure. *Journal of Geophysical Research*, 110, Article C10016. <https://doi.org/10.1029/2004JC002788>
- Luhar, M., Coutu, S., Infantes, E., Fox, S., & Nepf, H. (2010). Wave-induced velocities inside a model seagrass bed. *Journal of Geophysical Research: Oceans*, 115(C12), Article C12005, 1–15. <https://doi.org/10.1029/2010JC006345>
- Madsen, P. A., & Fuhrman, D. R. (2006). Third-order theory for bichromatic bi-directional water waves. *Journal of Fluid Mechanics*, 557, 369–397. <https://doi.org/10.1017/S0022112006009815>
- Mendez, F. J., Losada, I. J., Dalrymple, R. A., & Losada, M. A. (1998). Effects of wave reflection and dissipation on wave-induced second order magnitudes. *Proceeding to Coastal Engineering Conference, I*, 537–550. <https://doi.org/10.1061/9780784404119.039>
- Méndez, F. J., Losada, I. J., & Losada, M. A. (1999). Hydrodynamics induced by wind waves in a vegetation field. *Journal of Geophysical Research: Oceans*, 104(C8), 18383–18396. <https://doi.org/10.1029/1999JC900119>
- Möller, I., Kudella, M., Rupprecht, F., Spencer, T., Paul, M., Van Wesenbeeck, B. K., Wolters, G., Kai, J., Bouma, T. J., Miranda-Lange, M., & Schimmels, S. (2014). Wave attenuation over coastal salt marches under storm surge conditions. *Nature Geoscience*, 7, 727–731. <https://doi.org/10.1038/ngeo2251>
- Morris, R. L., Konlechner, T. M., Ghisalberti, M., & Swearer, S. (2018). From grey to green: Efficacy of eco-engineering solutions for nature-based coastal defence. *Global Change Biology*, 24(5), 1827–1842. <https://doi.org/10.1111/gcb.2018.24.issue-5>
- Mullarney, J. C., & Henderson, S. M. (2018). Flows Within Marine Vegetation Canopies, Chapter 1. In *Advances in Coastal Hydraulics* (pp. 1–46). World Scientific.
- Nakayama, A., & Kuwahara, F. (1999). A macroscopic turbulence model for flow in a porous medium. *Journal of Fluids Engineering – Transactions of the ASME*, 121(2), 427–433. <https://doi.org/10.1115/1.2822227>
- Nepf, H. M. (2012). Flow and transport in regions with aquatic vegetation. *Annual Review of Fluid Mechanics*, 44(1), 123–142. <https://doi.org/10.1146/fluid.2012.44.issue-1>
- Neshamar, O. E. (2022). *Hydrodynamics of oscillatory flow over an array of cylinders* [PhD thesis, University of Aberdeen].
- Neshamar, O. E., van der A, D. A., & O'Donoghue, T. (2022). Flow-induced vibration of a cantilevered cylinder in oscillatory flow at high KC. *Journal of Fluids and Structures*, 109, Article 103476. <https://doi.org/10.1016/j.jfluidstructs.2021.103476>
- O'Donoghue, T., & Wright, S. (2004). Flow tunnel measurements of velocities and sand flux in oscillatory sheet flow for well-sorted and graded sands. *Coastal Engineering*, 51(11), 1163–1184. <https://doi.org/10.1016/j.coastaleng.2004.08.001>
- Philips, O. M. (1980). *The dynamics of the upper ocean* (2nd ed., 1st paperback ed.). Cambridge monographs on mechanics and applied mathematics. Press Syndicate of the University of Cambridge.
- Pujol, D., Serra, T., Colomer, J., & Casamitjana, X. (2013). Flow structure in canopy models dominated by progressive waves. *Journal of Hydrology*, 486, 281–292. <https://doi.org/10.1016/j.jhydrol.2013.01.024>
- Rienecker, M. M., & Fenton, J. D. (1981). A Fourier approximation method for steady water-waves. *Journal of Fluid Mechanics*, 104, 119–137. <https://doi.org/10.1017/S0022112081002851>
- Schoonees, T., Mancheão, A. G., Scheres, B., Bouma, T. J., Silva, R., Schlurmann, T., & Schüttrumpf, H. (2019). Hard structures for coastal protection, towards greener designs. *Estuaries and Coasts*, 42(7), 1709–1729. <https://doi.org/10.1007/s12237-019-00551-z>
- Sollitt, C. K., & Cross, R. H. (1972). Wave transmission through permeable breakwaters. *Proceeding to Coastal Engineering Conference, III*, 1827–1846. <https://doi.org/10.1061/9780872620490.106>

Sumer, B. M., & Fredsøe, J. (1999). *Hydrodynamics around cylindrical structures* (1st ed.). Vol. 12 of *Advanced series on coastal engineering*. World Scientific.

Svendsen, I. A., & Jonsson, I. G. (1982). *Hydrodynamics of coastal regions* (1st, 2nd reprint ed.). Den Private Ingeniør-fond.

The European Commission (2021). *Evaluating the impact of nature-based solutions: A handbook for practitioners*. Publications Office of the European Union.

The World Bank (2017). *Implementing nature-based flood protection – principles and implementation guidance* (1st ed.). The World Bank.

Tinoco, R. O., & Coco, G. (2014). Observations of the effect of emergent vegetation on sediment resuspension under unidirectional currents and waves. *Earth Surface Dynamics*, 2(1), 83–96. <https://doi.org/10.5194/esurf-2-83-2014>

Tinoco, R. O., & Coco, G. (2018). Turbulence as the main driver of resuspension in oscillatory flow through vegetation. *Journal of Geophysical Research – Earth Surface*, 123, 1–14. <https://doi.org/10.1002/jgrf.v123.5>

Van Rooijen, A., Lowe, R., Rijnsdorp, D. P., Ghisalberti, M., Jacobsen, N. G., & McCall, R. (2020). Wave-driven mean flow dynamics in submerged canopies. *Journal of Geophysical Research: Oceans*, 125, Article e2019JC015935. <https://doi.org/10.1029/2019JC015935>

Yang, J. Q., Chung, H., & Nepf, H. M. (2016). The onset of sediment transport in vegetated channels predicted by turbulent kinetic energy. *Geophysical Research Letters*, 43(21), 1–8. <https://doi.org/10.1002/2016GL071092>

Zeller, R. B., Zarama, F. J., Weitzman, J. S., & Koseff, J. R. (2015). A simple and practical model for combined wave-current canopy flows. *Journal of Fluid Mechanics*, 767, 842–880. <https://doi.org/10.1017/jfm.2015.59>

Appendix A. Derivation of bulk formulation

A.1 Porous media formulation for pure oscillating flow

It is discussed in Section 2.1 that the vertical momentum equation for the spatially-averaged vertical velocity w simplifies to:

$$\frac{\partial p}{\partial z} = 0 \quad (\text{A1})$$

because $w = 0$ given the form of the continuity equation for oscillatory motion (Eq. (1)). Consequently, focus is given to the derivation of the horizontal momentum equation Eq. (2). The horizontal momentum equation reads as follows (Jensen et al., 2014, with the present work’s formulation of drag and

inertia resistance):

$$\begin{aligned} & \left(1 + C_m N \frac{d^2}{4\pi}\right) \frac{\partial u}{\partial t} + \frac{1}{n} \left[\frac{\partial n^{-1}uu}{\partial x} + \frac{\partial n^{-1}uv}{\partial y} + \frac{\partial n^{-1}uw}{\partial z} \right] \\ & = -\frac{1}{\rho} \frac{\partial p}{\partial x} + \frac{1}{n} \frac{\partial}{\partial z} \left[(v + v_t) \left(\frac{\partial u}{\partial z} + \frac{\partial w}{\partial x} \right) \right] - F_D \quad (\text{A2}) \end{aligned}$$

where horizontal diffusion terms are already ignored, since all derivatives along x and y vanish for spatially-averaged quantities. In the same way, the first two convective terms can be removed. The third convective term vanishes, since $w = 0$ given the bottom boundary condition and the continuity equation (Eq. (1)). Finally, the diffusion term proportional to $\partial w/\partial x$ vanishes (again, since $w = 0$ for all z). This results in the horizontal momentum equations in Eq. (2).

A.2 Bulk two-layer model

The bulk two-layer model is found by a vertical averaging of Eq. (2) over the canopy height:

$$\begin{aligned} \frac{1}{h_v} \int_0^{h_v} \left[\Gamma_I \frac{\partial u}{\partial t} = -\frac{1}{\rho} \frac{\partial p}{\partial x} + \frac{1}{n} \frac{\partial}{\partial z} (v + v_t) \frac{\partial u}{\partial z} \right. \\ \left. - \frac{1}{2} C_D P(n) N d |u| u \right] dz \quad (\text{A3}) \end{aligned}$$

and introduction of the bulk velocity:

$$U = \frac{1}{h_v} \int_0^{h_v} u \, dz \quad (\text{A4})$$

The first two terms in Eq. (A3) become $\Gamma_I \partial U/\partial t$ and $\frac{1}{\rho} \partial p/\partial x$, respectively, as per Eq. (5): the first term, because $\partial/\partial t$ can be taken outside the integral, and the second term, because p is independent of z . The only horizontal shear terms acting on the control volume bounding the vegetation are on the seabed and the top of the canopy, which are lumped into a single shear term $\tau = C_f |\Delta U| \Delta U$ (see Section 2.1 for a discussion on this parameterization). However, since Eq. (A3) is averaged over the canopy height it follows that:

$$\frac{1}{h_v} \int_0^{h_v} \frac{1}{n} \frac{\partial}{\partial z} (v + v_t) \frac{\partial u}{\partial z} \, dz = \frac{C_f}{h_v} |\Delta U| \Delta U \quad (\text{A5})$$

Finally, the drag term reads:

$$\frac{1}{2} C_D P(n) N d \frac{1}{h_v} \int_0^{h_v} |u| u \, dz = \frac{1}{2} C_D P(n) N d \frac{\alpha_U |U| U h_v}{h_v} \quad (\text{A6})$$

Here, α_U is the shape factor accounting for the slight deviations from the near-constant in-canopy velocity profile (Fig. 10); α_U is in practice lumped into C_D , when C_D is derived from the experimental results.